against 30 mM Tris–HCl (pH 7.5) to remove H_2O_2. To identify the modification, inhibitor-bound α-synuclein monomer and dimer, as well as H_2O_2-treated α-synuclein, were incubated with trypsin at 37 °C for 18 h at an enzyme-to-substrate ratio of 1:50 (mol/mol) in 30 mM Tris–HCl (pH 7.5). Digested peptide products were separated by reverse-phase HPLC on a Supersphere Select B column (2.1 × 125 mm; Merck) and analyzed by MALDI-TOF MS.

Determination of stoichiometry of exifone/α-synuclein complexes

The stoichiometry of exifone/α-synuclein complexes was determined by measuring the absorbance of exifone at 385 nm using a spectrophotometer (UV-1600 PC, Shimadzu Co). Exifone-bound monomeric and dimeric α-synucleins were isolated by gel-filtration chromatography as described above.

Redox-cycle staining

Samples were subjected to SDS-PAGE and transferred onto polyvinylidene fluoride membranes. The membranes were incubated in 0.24 mM NBT (Sigma), 2 M potassium glycinate solution (pH 10.0) in the dark for 16 h at room temperature and then dipped in 100 mM sodium borate (pH 10.0). Exifone-bound α-synuclein was specifically stained as purple-blue bands due to NBT reduction to formazan.

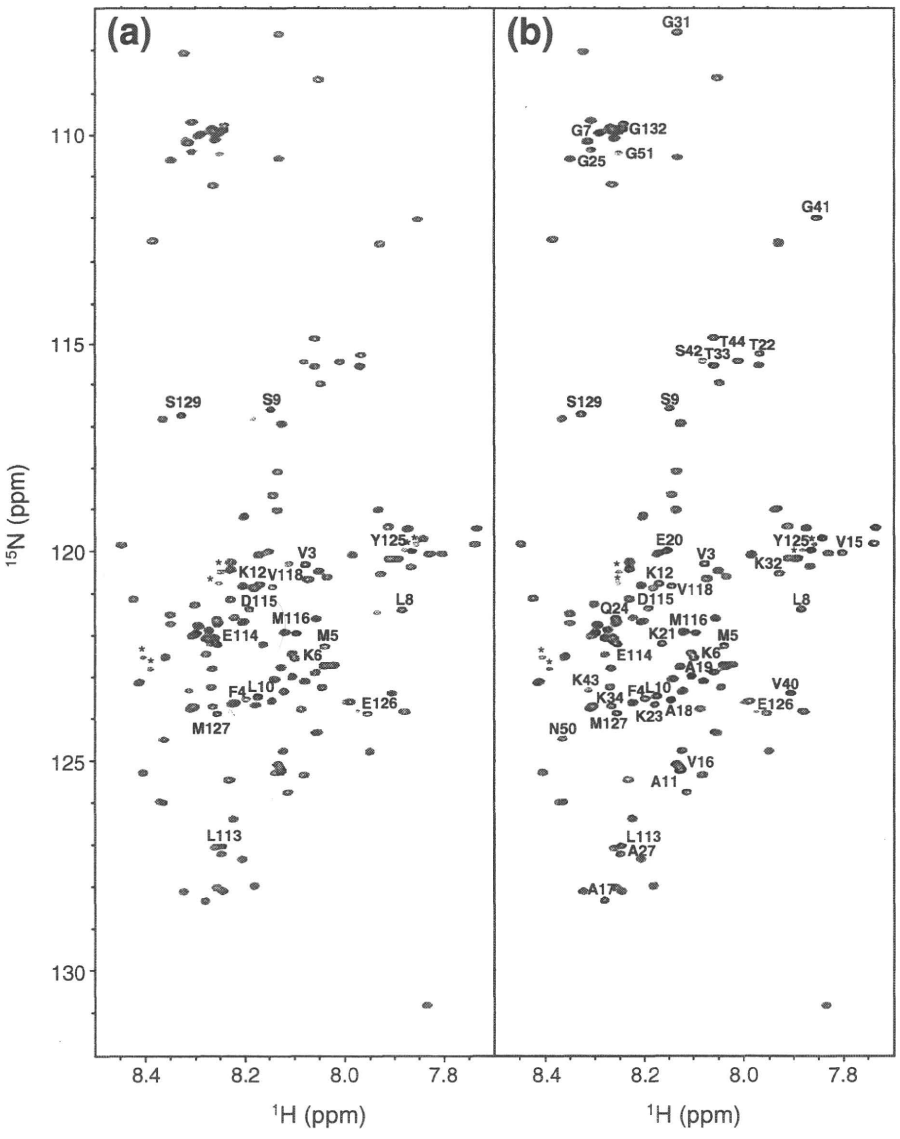

Fig. 6. NMR spectral comparison of exifone-bound ^{15}N-labeled α-synuclein dimer and control monomer. (a) ^{1}H–^{15}N HSQC spectra of ^{15}N-labeled Exi-monomer (red) and ^{15}N-labeled control monomer (black) recorded at a proton frequency of 920 MHz. (b) ^{1}H–^{15}N HSQC spectra of ^{15}N-labeled Exi-dimer (red) and ^{15}N-labeled control monomer (black). (c) Plot of the relative peak intensities, I(Exi-monomer)/I(monomer), of the HSQC cross-peaks in the Exi-monomer and control monomer *versus* the amino acid sequence of α-synuclein. (d) I(Exi-dimer)/I(monomer) of the HSQC cross-peaks in the Exi-dimer and control monomer. Signals derived from oxidized methionines and their neighboring residues (indicated with asterisks in a and b) were split and not taken into account. The peak splittings mostly reflect a mixture of *R* and *S* isomers of methionine sulfoxide.[18]

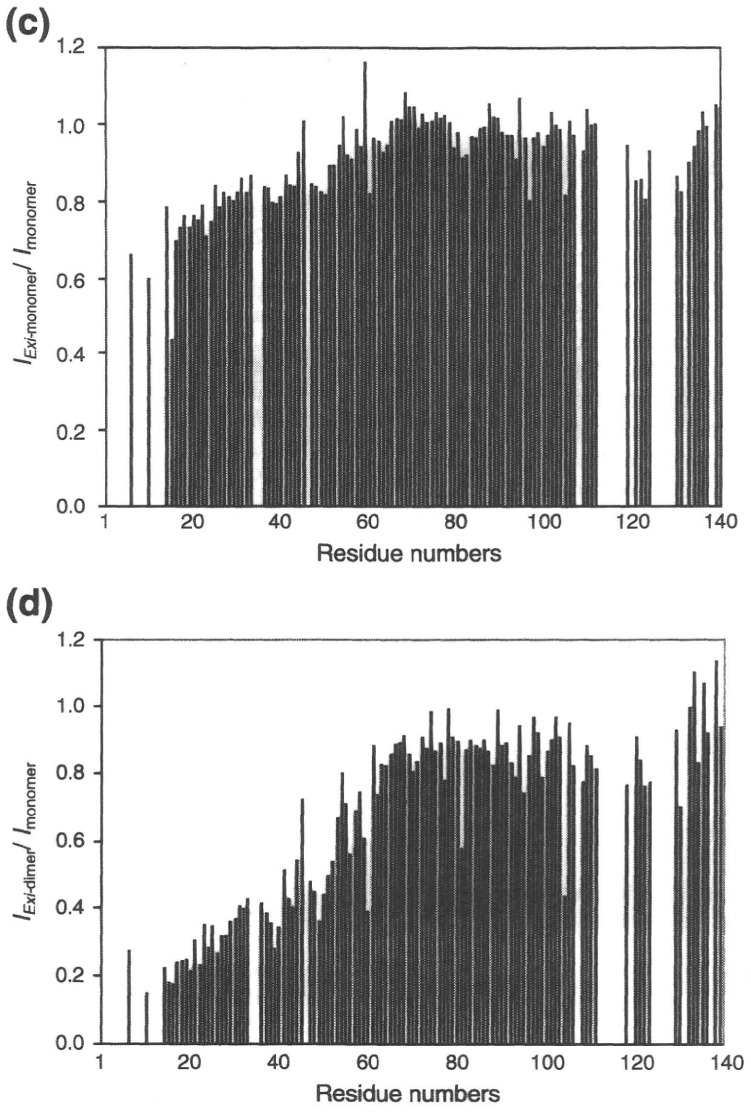

Fig. 6 *(legend on previous page)*

Asp-N digestion of α-synuclein dimer

α-Synuclein dimer (0.25 mg/mL) in 30 mM Tris–HCl (pH 7.5) was treated with 40 μg/mL of Asp-N (Roche) at 37 °C for 1 h. The reaction was stopped by adding 2× SDS sample buffer [4% SDS, 0.16 M Tris–HCl (pH 6.8), 30% glycerol] and the solution was boiled for 5 min. The samples were loaded onto 15% Tris/tricine SDS-PAGE gel, and the digested products were detected by silver staining (kit from Wako), immunoblotting, and redox-cycling staining. For immunoblotting, SDS-PAGE gels were blotted onto polyvinylidene fluoride membranes, blocked with 3% gelatin/phosphate-buffered saline, and incubated overnight at room temperature with anti-α-synuclein antibody in 10% FBS/phosphate-buffered saline. After washing, the blots were incubated for 2 h at room temperature with biotinylated secondary antibody (1:500) (Vector Laboratories). Following further washing, the blots were incubated with peroxidase-labeled avidin–biotin (Vector laboratories) for 30 min at room temperature and developed with $NiCl_2$-enhanced diaminobenzidine (Sigma).

NMR measurements

The samples for NMR experiments were prepared at a concentration of 0.1–1.0 mM in 90% H_2O/10% D_2O (v/v), 10 mM sodium phosphate buffer, and 100 mM NaCl at pH 7.0. NMR experiments were performed at 10 °C using a JEOL JNM-ECA920 spectrometer equipped with a 5-mm triple resonance probe. Backbone assignments of α-synuclein monomer were achieved by means of standard triple resonance experiments, as described previously.[13] The samples were checked by SDS-PAGE before and after NMR measurements, and it was confirmed that aggregation of inhibitor-bound α-synuclein monomer and dimer did not occur under these conditions. NMR time domain data were processed with the nmrPipe package[22] and the spectra were analyzed by using

Sparky software (T. D. Goddard and D. G. Kneller, University of California, San Francisco).

Acknowledgements

We thank K. Senda and K. Hattori (Nagoya City University) for help in the preparation of the recombinant proteins for NMR spectroscopy. We also thank M. Nakano (IMS) and T. Sugihara (JEOL) for help in NMR measurements and K. Matsumoto (RIKEN) for assistance in MS. We thank Drs. H. Sezaki, A. Hayashi, and T. Hosono (Agilent Technologies Japan) for their kind support in liquid chromatography–electrospray ionization MS analysis. This work was supported in part by Grants-in-Aid for Scientific Research on Priority Areas, Research on Pathomechanisms of Brain Disorders (to Y.Y., K.K., and M.H.), Grants-in-Aid for Scientific Research on Innovative Areas, Molecular Science of Fluctuations toward Biological Functions (to K.K.), and "Nanotechnology Network Project" of the Ministry of Education, Culture, Sports, Science and Technology (MEXT). This work was also supported by Takeda Science Foundation (Y.Y.).

Supplementary Data

Supplementary data associated with this article can be found, in the online version, at doi:10.1016/j.jmb.2009.10.068

References

1. Conway, K. A., Rochet, J. C., Bieganski, R. M. & Lansbury, P. T., Jr (2001). Kinetic stabilization of the α-synuclein protofibril by a dopamine-α-synuclein adduct. *Science*, **294**, 1346–1349.
2. Li, H. T., Lin, D. H., Luo, X. Y., Zhang, F., Ji, L. N., Du, H. N. *et al.* (2005). Inhibition of α-synuclein fibrillization by dopamine analogs via reaction with the amino groups of α-synuclein. Implication for dopaminergic neurodegeneration. *FEBS J.* **272**, 3661–3672.
3. Masuda, M., Suzuki, N., Taniguchi, S., Oikawa, T., Nonaka, T., Iwatsubo, T. *et al.* (2006). Small molecule inhibitors of α-synuclein filament assembly. *Biochemistry*, **45**, 6085–6094.
4. Porat, Y., Abramowitz, A. & Gazit, E. (2006). Inhibition of amyloid fibril formation by polyphenols: structural similarity and aromatic interactions as a common inhibition mechanism. *Chem. Biol. Drug Des.* **67**, 27–37.
5. Feng, B. Y., Toyama, B. H., Wille, H., Colby, D. W., Collins, S. R., May, B. C. *et al.* (2008). Small-molecule aggregates inhibit amyloid polymerization. *Nat. Chem. Biol.* **4**, 197–199.
6. Norris, E. H., Giasson, B. I., Hodara, R., Xu, S., Trojanowski, J. Q., Ischiropoulos, H. & Lee, V. M. (2005). Reversible inhibition of α-synuclein fibrillization by dopaminochrome-mediated conformational alterations. *J. Biol. Chem.* **280**, 21212–21219.
7. Herrera, F. E., Chesi, A., Paleologou, K. E., Schmid, A., Munoz, A., Vendruscolo, M. *et al.* (2008). Inhibition of α-synuclein fibrillization by dopamine is mediated by interactions with five C-terminal residues and with E83 in the NAC region. *PLoS ONE*, **e3394**, 3.
8. Ehrnhoefer, D. E., Bieschke, J., Boeddrich, A., Herbst, M., Masino, L., Lurz, R. *et al.* (2008). EGCG redirects amyloidogenic polypeptides into unstructured, off-pathway oligomers. *Nat. Struct. Mol. Biol.* **15**, 558–566.
9. Moussa, C. E., Mahmoodian, F., Tomita, Y. & Sidhu, A. (2008). Dopamine differentially induces aggregation of A53T mutant and wild type α-synuclein: insights into the protein chemistry of Parkinson's disease. *Biochem. Biophys. Res. Commun.* **365**, 833–839.
10. Rao, J. N., Dua, V. & Ulmer, T. S. (2008). Characterization of α-synuclein interactions with selected aggregation-inhibiting small molecules. *Biochemistry*, **47**, 4651–4656.
11. Hong, D. P., Fink, A. L. & Uversky, V. N. (2008). Structural characteristics of α-synuclein oligomers stabilized by the flavonoid baicalein. *J. Mol. Biol.* **383**, 214–223.
12. Masuda, M., Hasegawa, M., Nonaka, T., Oikawa, T., Yonetani, M., Yamaguchi, Y. *et al.* (2009). Inhibition of α-synuclein fibril assembly by small molecules: analysis using epitope-specific antibodies. *FEBS Lett.* **583**, 787–791.
13. Sasakawa, H., Sakata, E., Yamaguchi, Y., Masuda, M., Mori, T., Kurimoto, E. *et al.* (2007). Ultra-high field NMR studies of antibody binding and site-specific phosphorylation of α-synuclein. *Biochem. Biophys. Res. Commun.* **363**, 795–799.
14. Uversky, V. N., Yamin, G., Souillac, P. O., Goers, J., Glaser, C. B. & Fink, A. L. (2002). Methionine oxidation inhibits fibrillation of human α-synuclein *in vitro*. *FEBS Lett.* **517**, 239–244.
15. Paz, M. A., Gallop, P. M., Torrelio, B. M. & Fluckiger, R. (1988). The amplified detection of free and bound methoxatin (PQQ) with nitroblue tetrazolium redox reactions: insights into the PQQ-locus. *Biochem. Biophys. Res. Commun.* **154**, 1330–1337.
16. Ingrosso, D., Fowler, A. V., Bleibaum, J. & Clarke, S. (1989). Specificity of endoproteinase Asp-N (Pseudomonas fragi): cleavage at glutamyl residues in two proteins. *Biochem. Biophys. Res. Commun.* **162**, 1528–1534.
17. Tetaz, T., Morrison, J. R., Andreou, J. & Fidge, N. H. (1990). Relaxed specificity of endoproteinase Asp-N: this enzyme cleaves at peptide bonds N-terminal to glutamate as well as aspartate and cysteic acid residues. *Biochem. Int.* **22**, 561–566.
18. Stadtman, E. R., Van Remmen, H., Richardson, A., Wehr, N. B. & Levine, R. L. (2005). Methionine oxidation and aging. *Biochim. Biophys. Acta*, **1703**, 135–140.
19. Rospigliosi, C. C., McClendon, S., Schmid, A. W., Ramlall, T. F., Barre, P., Lashuel, H. A. & Eliezer, D. (2009). E46K Parkinson's-linked mutation enhances C-terminal-to-N-terminal contacts in α-synuclein. *J. Mol. Biol.* **388**, 1022–1032.
20. Jakes, R., Spillantini, M. G. & Goedert, M. (1994). Identification of two distinct synucleins from human brain. *FEBS Lett.* **345**, 27–32.
21. Masuda, M., Dohmae, N., Nonaka, T., Oikawa, T., Hisanaga, S., Goedert, M. & Hasegawa, M. (2006). Cysteine misincorporation in bacterially expressed human α-synuclein. *FEBS Lett.* **580**, 1775–1779.
22. Delaglio, F., Grzesiek, S., Vuister, G. W., Zhu, G., Pfeifer, J. & Bax, A. (1995). NMRPipe: a multidimensional spectral processing system based on UNIX pipes. *J. Biomol. NMR*, **6**, 277–293.

THE JOURNAL OF BIOLOGICAL CHEMISTRY VOL. 285, NO. 29, pp. 22221–22231, July 16, 2010

Mutation-dependent Polymorphism of Cu,Zn-Superoxide Dismutase Aggregates in the Familial Form of Amyotrophic Lateral Sclerosis*[S]

Received for publication, February 11, 2010, and in revised form, April 16, 2010 Published, JBC Papers in Press, April 19, 2010, DOI 10.1074/jbc.M110.113597

Yoshiaki Furukawa[‡1,2], **Kumi Kaneko**[‡], **Koji Yamanaka**[§], **and Nobuyuki Nukina**[‡3]

From the [‡]*Laboratory for Structural Neuropathology and* [§]*Laboratory for Motor Neuron Disease, RIKEN Brain Science Institute, Wako, Saitama 351-0198, Japan*

More than 100 different mutations in Cu,Zn-superoxide dismutase (SOD1) are linked to a familial form of amyotrophic lateral sclerosis (fALS). Pathogenic mutations facilitate fibrillar aggregation of SOD1, upon which significant structural changes of SOD1 have been assumed; in general, however, a structure of protein aggregate remains obscure. Here, we have identified a protease-resistant core in wild-type as well as fALS-causing mutant SOD1 aggregates. Three different regions within an SOD1 sequence are found as building blocks for the formation of an aggregate core, and fALS-causing mutations modulate interactions among these three regions to form a distinct core, namely SOD1 aggregates exhibit mutation-dependent structural polymorphism, which further regulates biochemical properties of aggregates such as solubility. Based upon these results, we propose a new pathomechanism of fALS in which mutation-dependent structural polymorphism of SOD1 aggregates can affect disease phenotypes.

Misfolding of a protein molecule often causes its insoluble aggregation, and formation of inclusion bodies containing protein aggregates is a major pathological change in conformational diseases such as neurodegenerative disorders (1). Increasing evidence has suggested that structures/morphologies of protein aggregates affect disease phenotypes and that polymorphism of protein aggregates associates with phenotypic heterogeneity (2–5). Distinct molecular structures of protein aggregates will therefore play an important role in expression of different phenotypes observed in conformational diseases.

Among neurodegenerative disorders, more than a hundred dominant mutations in Cu,Zn-superoxide dismutase (SOD1) have been identified to cause a familial form of amyotrophic lateral sclerosis (fALS)[4] (6). SOD1 binds a copper and a zinc ion and forms an intramolecular disulfide bond (7), all of which tightly regulate an antioxidant activity of SOD1 that converts superoxide into oxygen and hydrogen peroxide (8). SOD1 knock-out mice, however, show no fALS-like phenotypes, suggesting that an enzymatic role of SOD1 makes a minor contribution to neurodegeneration (9). Instead, SOD1 has been considered to gain toxic properties by fALS mutations, and one of those is the increased propensity of protein misfolding and aggregation (10). Among all SOD1-related fALS, a common pathological change is accumulation of detergent-insoluble SOD1 aggregates in spinal cords (10).

So far, much effort has been made to reveal a general mechanism of how >100 fALS mutations promote SOD1 aggregation. Most of fALS mutations destabilize a native structure of SOD1 (11, 12), which retards either metal binding or disulfide formation in SOD1 (13–15). A pathogenic consequence common to all fALS mutations in SOD1 has hence been proposed to increase an intracellular fraction of a metal-free SOD1 without a disulfide (apo-SOD1^{SH}), which is the most aggregation-prone state (13). Overall structures of SOD1 appear to be preserved even after demetallation and disulfide reduction, but a significant structural disorder in the loop regions has been identified in soluble apo-SOD1^{SH} (16). Such increased mobility of the loop regions in the apo-SOD1^{SH} state has been considered to promote non-native interactions between SOD1s (17), possibly leading to insoluble aggregation.

During the aggregate formation, apo-SOD1^{SH} has been predicted to undergo drastic structural changes, which include three-dimensional rearrangement of β-sheets called domain swapping (18). However, there is little experimental evidence to unveil the structure(s) that an SOD1 molecule adopts in the insoluble aggregates. In addition, less attention has been paid so far on any possible differences in structural properties among SOD1 aggregates with different fALS mutations. Given that aggregate polymorphism associates with different disease phenotypes in the other neurodegenerative disorders such as prion diseases (2, 3), an assumption on a "mutation-independent" structure of SOD1 aggregates should now be carefully examined; indeed, phenotypic heterogeneity has been reported in fALS patients with different SOD1 mutations (19).

* This work was supported by Grant-in-aid for Scientific Research on Priority Areas (Research on Pathomechanisms of Brain Disorders) 17025044 (to N. N.), Grants-in-aid 20770130 (to Y. F.) and 21390274 (to K. Y.) from the Ministry of Education, Culture, Sports, Science and Technology of Japan, and a Health and Labour Science Research grant (to K. Y.).

[S] The on-line version of this article (available at http://www.jbc.org) contains supplemental Table 1 and Figs. S1–S4.

[1] To whom correspondence may be addressed: 3-14-1 Hiyoshi, Kohoku, Yokohama 223-8522, Japan. Fax: 81-45-566-1697; E-mail: furukawa@chem.keio.ac.jp.

[2] Present address: Dept. of Chemistry, Keio University, 3-14-1 Hiyoshi, Kohoku, Yokohama 223-8522, Japan.

[3] To whom correspondence may be addressed: 2-1 Hirosawa, Wako, Saitama 351-0198, Japan. Fax: 81-48-462-4796; E-mail: nukina@brain.riken.jp.

[4] The abbreviations used are: fALS, familial form of amyotrophic lateral sclerosis; DTT, dithiothreitol; ThT, thioflavin T; WT, wild type; MALDI-TOF, matrix-assisted laser desorption ionization time-of-flight; MS/MS, tandem mass spectrometry; TCEP, tris(2-carboxyethyl)phosphine.

In this study, we have experimentally identified a protease-resistant core structure in the SOD1 aggregates and found that three different regions (amino acids 1–30, 90–120, and 135–153) within an SOD1 primary sequence form a scaffold of a core in the aggregates. Interestingly, fALS mutations in SOD1 can modulate interactions of those three scaffold regions in a core structure, which produces mutation-dependent structural polymorphism of SOD1 aggregates. Furthermore, such mutation-dependent core structures lead to distinct morphological and biochemical properties of fALS-mutant SOD1 aggregates. Based upon this study, we propose a new pathomechanism of fALS in which mutation-dependent structures of SOD1 aggregates can affect the disease phenotypes.

EXPERIMENTAL PROCEDURES

Preparation of SOD1 Proteins—WT and fALS-mutant SOD1 cDNA were cloned in a multiple cloning site of a plasmid, pET15b (Novagen), using NdeI and SalI sites, where a SalI site is introduced between BamHI and Bpu1102I sites. SOD1 proteins were obtained as inclusion bodies in *Escherichia coli*, Rosetta, transformed with the above plasmid after induction with 1 mM isopropyl 1-thio-β-D-galactopyranoside at 37 °C for 6 h and purified using Proteus Midi IMAC (Pro-Chem Inc.) in the presence of 6 M guanidine hydrochloride. Purified SOD1 proteins were refolded by 100-fold dilution in a buffer containing 100 mM Na-P_i, 100 mM NaCl, 5 mM EDTA, pH 8.0 (NNE buffer), with 5 mM DTT and stirred at 4 °C overnight. Refolded protein samples were concentrated and ultracentrifuged at 110,000 × *g* for 30 min at 4 °C to remove insoluble materials. Protein concentration was spectroscopically determined from the absorbance at 280 nm (5,500 cm^{-1} M^{-1} of an extinction coefficient).

An N-terminal His tag in SOD1 was removed by treatment with thrombin immobilized with agarose (Calbiochem) in an NNE buffer at 37 °C at 100 rpm for an hour. After removal of immobilized thrombin by filtration and ultracentrifugation at 110,000 × *g* for 30 min, the protein concentration in a supernatant fraction was checked spectroscopically. Removal of a His tag was confirmed by SDS-PAGE as well as MALDI-TOF mass spectrometry (supplemental Fig. S1, *A–C*).

Characterization of SOD1 Aggregation—To examine aggregation of SOD1 proteins, 100 μM SOD1 in an NNE buffer containing 5 mM DTT was set in a 96-well plate and shaken at 37 °C at 1,200 rpm. Turbidity was monitored in a plate reader (ARVO MX, PerkinElmer Life Sciences) by measuring the absorbance around 405 nm. SOD1-insoluble aggregates were obtained as a pellet fraction after ultracentrifugation of the reaction mixtures at 110,000 × *g* for 30 min (supplemental Fig. S1*H*).

For the analysis of ThT fluorescence, SOD1 aggregates were resuspended in water with ultrasonication, and aliquots were loaded on an SDS-polyacrylamide gel and stained with Coomassie Brilliant Blue (supplemental Fig. S2*A*); thereby we can estimate SOD1 concentration (at a monomer basis) in aggregates. Using a 96-well plate, 3 μM SOD1 aggregates were then mixed with 25 μM ThT in an NNE buffer, and the fluorescence was measured in a plate reader (ARVO MX) with a CW lamp filter (440-nm cutoff) and an emission filter (486-nm cutoff).

To examine temperature dependence of solubility of SOD1 aggregates, 30 μM SOD1 aggregates were prepared in an NNE buffer containing 5 mM DTT and 1% Sarkosyl and incubated at either 37, 60, 80, or 100 °C for an hour. After ultracentrifugation at 110,000 × *g* for 30 min, a supernatant fraction was saved, and a pellet fraction was further redissolved in an NNE buffer with 2% SDS. Both fractions were then mixed with an SDS-PAGE sample buffer containing 5 mM TCEP, boiled, and loaded on a 12.5% SDS-polyacrylamide gel. Protein bands were visualized by staining with Coomassie Brilliant Blue, and intensity of SOD1 bands was analyzed by an ImageJ software. Band intensities of soluble and insoluble fractions are denoted as I_s and I_i, respectively, and the fraction solubilized, F (%), is calculated as $I_s/(I_s + I_i) \times 100$. F is then plotted against incubation temperature, T, and estimation of $T_{1/2}$ was performed by fitting the data (Fig. 5*C*) with a sigmoidal function using Igor Pro version 4.0 (Wavemetrics) as shown in Equation 1,

$$F = \frac{100}{1 + \exp\left(-\frac{T - T_{1/2}}{a}\right)} \quad \text{(Eq. 1)}$$

where a is a coefficient. Experiments were repeated three times to estimate errors.

Electron Microscopy—To observe fibrillar morphologies of SOD1 aggregates with an electron microscope, we performed seeding reactions of SOD1 fibrillation, which can avoid shearing fibrils, namely 10 μM SOD1 aggregates were mixed with 100 μM soluble SOD1 and left at 37 °C for 3 days. Insoluble pellets were then collected by ultracentrifugation at 110,000 × *g* for 30 min and resuspended in water. SOD1 aggregates were adsorbed on 400-mesh grids coated by a glow-charged supporting membrane. After washed with pure water, negative staining with 1% uranyl acetate was performed. Images were obtained using an electron microscope (1200EX, JEOL). The width of a fibrillar structure was measured using a Photoshop 7.0 software (Adobe), and 10 different fibrils were examined to estimate errors.

Identification of a Core Region in SOD1 Aggregates—22.5 μg of SOD1 aggregates were resuspended in 100 μl of 50 mM Tris, 100 mM NaCl, 5 mM $CaCl_2$, pH 8.0, mixed with 5 μg of Pronase (Calbiochem) and incubated at 37 °C for an hour. After ultracentrifugation at 110,000 × *g* for 30 min, supernatants were discarded, and the pellets were washed once with 150 μl of 50 mM Tris, 100 mM NaCl, pH 8.0. The final pellets were redissolved in 20 μl of 50 mM Tris, 500 mM NaCl, 6 M guanidine HCl, 5 mM EDTA, 5 mM DTT, pH 8.0, and desalted using NuTip C-18 (Glygen Co.). α-Cyano-4-hydroxycinnamic acid was chosen as a matrix, and MALDI-MS and MS/MS spectra were acquired using a 4800plus MALDI-TOF/TOF Analyzer (Applied Biosystems). Identification of peptides based upon the observed m/z values was performed using PAWS software (ProteoMetrics).

For modifications of SOD1 aggregates with Alexa555, 60 μM SOD1 aggregate was mixed with 300 μM Alexa555 in an NNE buffer containing 5 mM TCEP and incubated at room temperature for an hour in the dark. After ultracentrifugation at

110,000 × *g* for 30 min, the pellets were washed once with an NNE buffer and resuspended and sonicated in 10 mM Tris-HCl, pH 8.0, with 4 M urea. Modifications of soluble SOD1 with Alexa555 were also performed by incubating 60 μM SOD1 with 300 μM Alexa555 in an NNE buffer containing 5 mM TCEP. Followed by addition of 20% trichloroacetic acid, which quenches the modification reaction, the sample solution was centrifuged at 20,000 × *g* for 10 min. The pellets were washed once with acetone and redissolved in 10 mM Tris-HCl, pH 8.0, with 4 M urea.

To identify the modification sites in SOD1, 4.5 μg of soluble or aggregated SOD1 with or without Alexa555 modification was incubated with 0.1 μg of lysyl endopeptidase (Wako) in 10 mM Tris-HCl, pH 8.0, with 4 M urea. The samples were incubated at 30 °C for an hour, desalted/purified with NuTip C-18, and analyzed by a 4800plus MALDI-TOF/TOF analyzer. Although a chemical structure of Alexa555-C_2-maleimide has not been available, we determined its mass (*m/z* 955.3, monoisotopic) by MALDI-TOF mass spectrometry.

Preparation of SOD1 Aggregates from Spinal Cords of Transgenic fALS Model Mice—Transgenic mice expressing SOD1 with G37R (established as LoxSOD1^{G37R} mice) (20), G85R (SOD1^{G85R}, a kind gift from Dr. Don Cleveland, University of California, San Diego) (21), and G93A (SOD1^{G93A}G1H, obtained from The Jackson Laboratory) (22) mutations were housed in the animal facility of RIKEN Brain Science Institute and sacrificed at the end-stage of disease. End-stage was determined by hindlimb paralysis so severe that the mouse could not right itself within 20 s when placed on its side, an end point frequently used for the mutant SOD1-expressing mice (20) and one that was consistent with the requirements of the Animal Experiment Committee of the RIKEN Brain Science Institute. Detergent extraction of SOD1 aggregates from these murine lumbar spinal cords was performed as reported previously (23). In short, spinal cords were homogenized in TEN buffer (10 mM Tris, 1 mM EDTA, 100 mM NaCl, pH 8.0) and centrifuged at 800 × *g* for 10 min to remove initial debris. 1:10 volume of TEN buffer with 10% Nonidet P-40 was then added to the supernatant, which was further sonicated and ultracentrifuged at 110,000 × *g* for 30 min. The resultant pellets were resuspended and sonicated in TEN buffer containing 0.5% Nonidet P-40, 0.25% SDS, and 0.5% deoxycholate and then ultracentrifuged at 110,000 × *g* for 30 min. Final pellets from lumbar spinal cords were resuspended and sonicated in 100 μl of pure water per mouse. Out of a total of 100 μl, 20 μl was used for Pronase digestion experiments, and 6 μl was used for solubility assay in the presence of 1% Sarkosyl.

RESULTS

Core Structure of SOD1 Fibrillar Aggregates—As shown in our recent studies (13), SOD1 forms fibrillar aggregates only when copper and zinc ions as well as a disulfide bond are absent (*i.e.* apo-SOD1^{SH}). To prepare SOD1 fibrillar aggregates, 100 μM soluble apo-SOD1^{SH} was agitated at 1,200 rpm at 37 °C, and the aggregation reaction was monitored by the increase of solution turbidity (see *WT* in supplemental Fig. S1*D*). After the turbidity change reached a plateau, a sample solution was separated by ultracentrifugation into supernatant and pellets. SOD1 was detected only in the pellet fraction (see *WT* in supplemental Fig. S1*H*), showing that all SOD1 molecules were converted into insoluble aggregates. Furthermore, SOD1-insoluble aggregates increase the ThT fluorescence (see *WT* in supplemental Fig. S2*C*) and red-shift the electronic absorption spectrum of Congo Red (supplemental Fig. S2*D*), both of which are typical tinctorial changes to indicate amyloid-like fibrillar structures in protein aggregates. These data thus confirm that apo-SOD1^{SH} forms amyloid-like fibrillar aggregates.

In general, protein fibrillar aggregates are composed of protease-resistant "core" and the associated "fuzzy coat" that is a susceptible region for proteolysis (24). We next attempted to identify which region(s) of an SOD1 amino acid sequence constitutes the protease-resistant core of SOD1 fibrillar aggregates. Apo-SOD1^{SH} aggregates prepared above were treated with a nonspecific protease, Pronase, to digest and remove the fuzzy coat regions, and the remaining insoluble pellets obtained by ultracentrifugation were supposed to be a protease-resistant core of SOD1 aggregates. Insoluble pellets after Pronase treatment were then solubilized in 6 M guanidine hydrochloride, and mass peaks were obtained by MALDI-TOF mass spectrometry (supplemental Fig. S3*A*); in contrast, no mass peaks were observed (*m/z* 1500–30,000, data not shown) when experiments were done in soluble apo-SOD1^{SH}. Based upon the observed mass with MS/MS analysis (supplemental Table S1), the peptides resistant to Pronase treatment are identified and mapped on an SOD1 primary sequence (Fig. 1*A*). As shown in Fig. 1*A*, multiple peptides are concentrated in one N-terminal (Ala^1–Lys^{30}, region A) and two C-terminal (Asp^{90}–His^{120}, region B; Thr^{135}–Gln^{153}, region C) regions. Soluble SOD1 has a three-dimensional structure with an immunoglobulin-fold comprising eight β-sheets, among which β1, β2, β6, β7, and β8 are involved in the formation of a core structure upon aggregation (Fig. 1*B*).

To further test if these three regions are responsible for SOD1 aggregation, four overlapping SOD1 peptide fragments N-terminally fused with a His_6 tag were prepared (Fig. 1*A*) as follows: Ala^1–Ala^{55} (ex1–2), Glu^{24}–Arg^{79} (ex2–3), Gly^{56}–Val^{118} (ex3–4), and His^{80}–Gln^{153} (ex4–5). Ex1–2 and ex4–5 peptides become insoluble after overnight agitation at 1,200 rpm, whereas ex2–3 and ex3–4 peptides remain in a supernatant fraction (Fig. 1*C*). Insoluble pellets of ex1–2 and ex4–5 but not a soluble form of these peptides increased the intensity of ThT fluorescence (Fig. 1*D*). By using an electron microscope, we have confirmed fibrillar morphology of ex1–2 and ex4–5 aggregates with ~9 nm of its width (Fig. 1, *E* and *F*). Taken these results together, we have revealed that non-native interactions among regions A–C form a core structure of SOD1 fibrillar aggregates.

Effects of fALS Mutations on SOD1 Fibrillar Aggregation—We next asked whether pathogenic mutations affect a molecular structure of SOD1 aggregates. As performed in WT SOD1, aggregates of mutant SOD1 were prepared by constant agitation of 100 μM mutant apo-SOD1^{SH}, and its aggregation reaction was monitored by the increase of solution turbidity (supplemental Fig. S1, *D–G*). Interestingly, not all of fALS

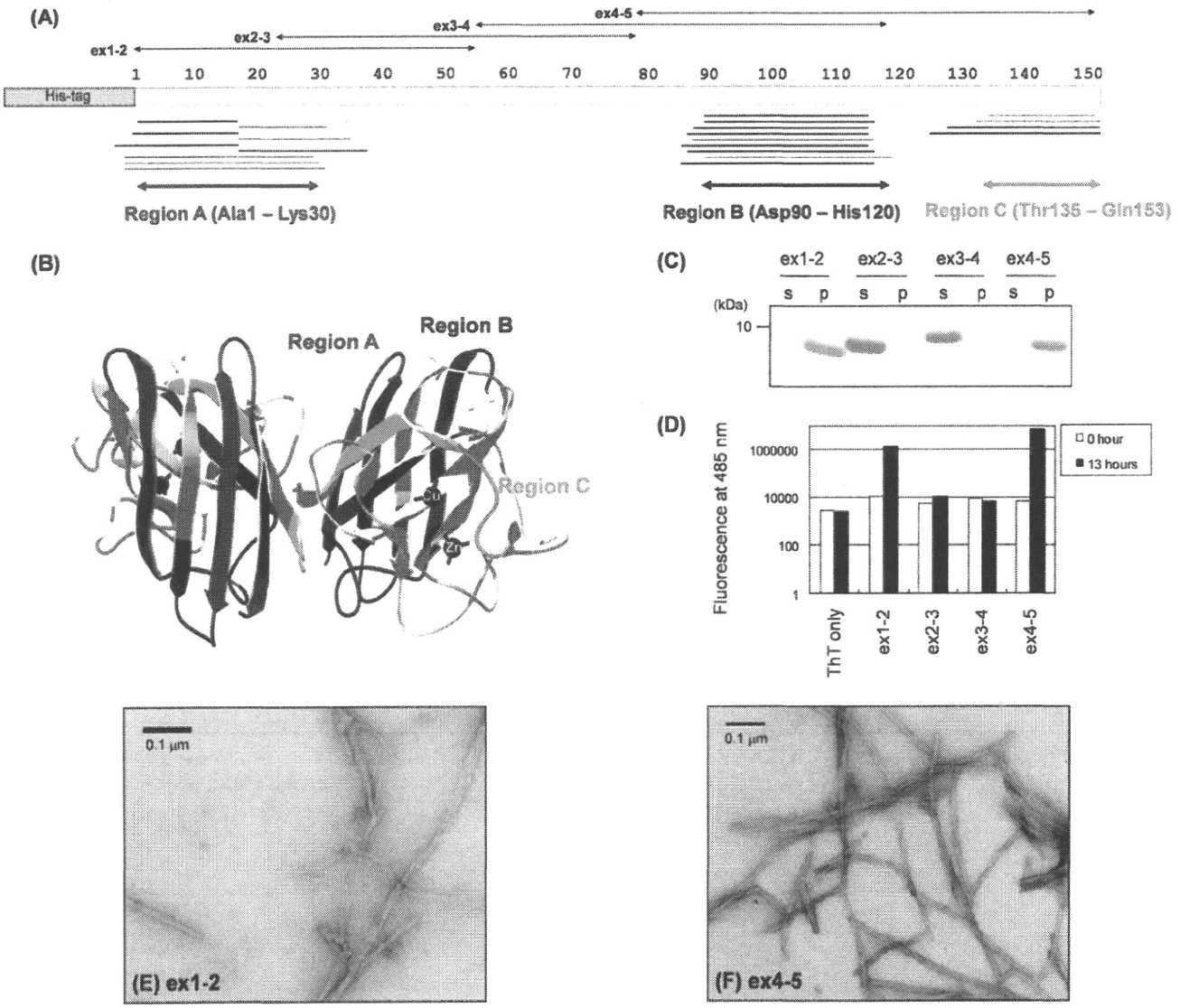

FIGURE 1. **MALDI-TOF mass spectrometric analysis of a core structure in SOD1 aggregate and experimental identification of SOD1 sequences with high aggregation propensities.** *A*, peptides corresponding to the mass peaks detected are mapped on the primary sequence of SOD1. *Numbers* indicated *above* the primary sequence of SOD1 (shown as *open bars*) represent the amino residue numbers. Peptides were identified either by MS/MS analysis (*thick bars*) or mass (*thin bars*). Details of peptide identification are summarized in supplemental Table S1. *B*, three-dimensional structure of an SOD1 dimer with copper and zinc ions bound (Protein Data Bank code 1HL5). Regions A–C are colored *red*, *blue*, and *green*, respectively. *C*, after overnight agitation of 100 μM SOD1 fragments (ex1–2, 2–3, 3–4, and 4–5 as shown in *A*) at 37 °C, a sample solution was ultracentrifuged at 110,000 × *g* for 30 min to separate a supernatant (*s*) and a pellet (*p*) fraction, and these fractions were analyzed by a 15% SDS-polyacrylamide gel stained with Coomassie Brilliant Blue. *D*, fluorescence intensity was measured in the samples containing 25 μM ThT and 3 μM SOD1 fragments before (0 h, *open bars*) and after (13 h, *filled bars*) 1,200 rpm agitation at 37 °C. *E* and *F*, electron micrograms of the pellet fraction containing (*E*) ex1–2 and (*F*) ex4–5 aggregates.

mutations accelerate the reaction of aggregate formation. Given that SOD1 aggregation is significantly suppressed by the presence of copper and zinc ions as well as a disulfide bond (13), aggregation kinetics of apo-SOD1^{SH} examined here (supplemental Fig. S1, *D–G*) will not correctly reflect that of SOD1 in the cellular environment where metal ions and disulfide bond could be introduced into mutant SOD1. Nonetheless, we would like to emphasize here that all mutant SOD1 proteins were eventually converted to insoluble aggregates when the turbidity change reached a plateau (supplemental Fig. S1*H*).

We have further confirmed the amyloid-like properties of mutant SOD1 aggregates by ThT fluorescence assay. After quantification of SOD1 aggregates by an SDS-PAGE analysis (supplemental Fig. S2, *A* and *B*), equal amounts of SOD1 aggregates were mixed with ThT (supplemental Fig. S2*C*). Although soluble SOD1 proteins showed no significant ThT fluorescence, all SOD1 aggregates tested here increased the intensity of ThT fluorescence, suggesting amyloid-like fibrillar structures in SOD1 aggregates. Furthermore, it is of note that each mutant SOD1 aggregate exhibits a distinct degree of the increase in the ThT fluorescence intensity (supplemental Fig. S2*C*). Given that the detailed mechanism of ThT binding to aggregates remains poorly understood, a molecular structure of the aggregate can hardly be inferred only from its ThT fluorescence intensity. These results, however, imply that each fALS-

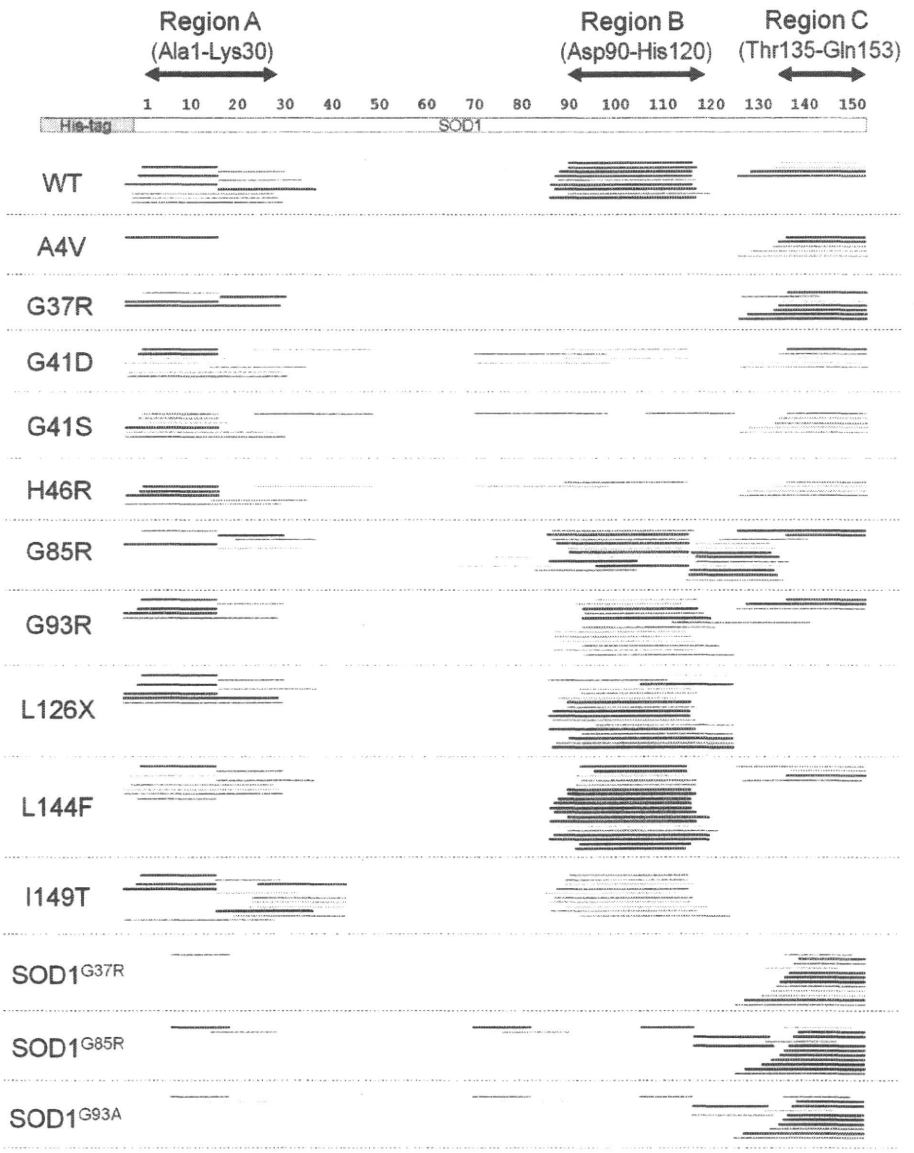

FIGURE 2. **Core regions in aggregates of WT and fALS-mutant SOD1 proteins identified by MALDI-TOF mass analysis.** $SOD1^{G37R}$, $SOD1^{G85R}$, and $SOD1^{G93A}$ indicate aggregates extracted from lumbar spinal cords of the corresponding transgenic mice, whereas the others are SOD1 aggregates prepared from the recombinant proteins with indicated fALS mutations. SOD1 aggregates were treated with Pronase, and the peptides resistant to digestion by Pronase were identified by MALDI-TOF mass spectrometry and mapped on the SOD1 primary sequence. *Numbers* indicated *above* the primary sequence of SOD1 (shown as an *open bar*) represent the amino residue numbers. Identification of mass peaks was performed based upon the observed mass values, and peptides shown as *thick bars* were further confirmed by MS/MS analysis. Details of peptide identification are summarized in supplemental Table S1 and supplemental Fig. S3, *L–O*.

mutant SOD1 forms an insoluble aggregate with distinct structural/biochemical properties.

Core Structure of SOD1 Aggregate Is Dependent upon fALS Mutations—To reveal mutational effects on a molecular structure of aggregated SOD1, we have again identified Pronase-resistant core structures in fALS-mutant SOD1 aggregates by using MALDI-TOF mass spectrometry (supplemental Fig. S3, *B–K* and supplemental Table S1). As summarized in Fig. 2, all mutant SOD1 aggregates contain an N-terminal region (region A) as a core structure, suggesting its primary role in SOD1 aggregation. This is consistent with a previous study showing that an SOD1 fragment from Ala^1 to Lys^{36} fused C-terminally with a yellow fluorescent protein forms aggregates in chick embryo spinal cord neural cells (25). In addition to such a common feature to all fALS-mutant SOD1s tested here, we noticed that a core structure in the aggregate is distinct among different fALS-mutant SOD1s and is classified into four types (Fig. 2 and Table 1). Type I includes WT and L144F, in which regions A–C include a core of aggregates. In A4V and G37R, which form type II aggregate, a core region is composed of regions A and C, but region B is not involved. G41D, G41S, and H46R can also be categorized as type II, in which the numbers of Pronase-resistant peptides covering region B were much less detected than those in the other types. Type III (G85R and G93R) shows a similar peptide map to type I, but a more extended C-terminal region participates in the formation of a core structure. In type IV (L126X and I149T), regions A and B but not C form a core in the aggregates. Although there may be more subtypes in the structural classification of SOD1 aggregates, our results have, for the first time, shown that fALS mutations can modulate non-native interactions among regions A–C to form distinct core structures in different mutant SOD1 aggregates.

We have also characterized Pronase-resistant peptides in the SOD1 aggregates extracted from lumbar spinal cords of transgenic mice expressing human SOD1 with G37R, G85R, and G93A mutations (supplemental Fig. S3, *L–O*). It is confirmed that regions A and C are involved in the core of all three *in vivo* SOD1 aggregates ($SOD1^{G37R}$, $SOD1^{G85R}$, and $SOD1^{G93A}$ in Fig. 2). In addition, a few peptides covering region B have been detected as aggregate core regions in *in vivo* $SOD1^{G85R}$ and $SOD1^{G93A}$ but not in *in vivo* $SOD1^{G37R}$ (Fig. 2). It is notable that no involvement of region B in the Pronase-resistant core is also characteristic of the *in vitro* G37R aggregates (see G37R in Fig. 2). Although maps of Pronase-resistant peptides are not precisely the same between *in vitro* and *in vivo* SOD1 aggregates, our results support some resemblance in the core regions between *in vivo* and *in vitro* SOD1 aggregates.

To get further insight into mutation-dependent structural polymorphism of SOD1 aggregates, we have tested reactivity of

TABLE 1
Properties of SOD1 aggregates are dependent upon fALS mutations

	Type	Width of fibrils	$T_{1/2}$	Average onset of disease[a]	Average duration of disease[a]
		nm	*°C*	*age*	*years*
WT	I	7.7 ± 1.1	57 ± 3.2		
A4V	II	3.3 ± 0.4	48 ± 5.8	47.7	1.2
G37R	II	3.1 ± 0.3	53 ± 1.9	36.9	17.0
G41D	II	ND[b]	63 ± 1.8	45.2	14.1
G41S	II	3.0 ± 0.4	63 ± 1.8	47.9	1.0
H46R	II	ND	52 ± 2.7	45.6	17.6
G85R	III	ND	60 ± 4.4	55.5	6.0
G93R	III	4.3 ± 0.4	62 ± 3.0	35.0	5.3
L126*X*	IV	11 ± 1.1	43 ± 0.1	42.0[c]	3.8[c]
L144F	I	8.3 ± 1.4	68 ± 1.4	54.6	11.8
I149T	IV	10 ± 0.9	42 ± 0.9	37.6	2.7

[a] Data are from Ref. 32.
[b] Data were not determined.
[c] Data are from Ref. 31.

four Cys residues (Cys^6, Cys^{57}, Cys^{111}, and Cys^{146}) in soluble and aggregated SOD1 proteins toward chemical modifications. Compared with Cys residues in a fuzzy coat of aggregates, we suppose that Cys residues buried in an aggregate core are less reactive toward a thiol-specific modifier, Alexa Fluor 555-C_2 maleimide (Alexa555), because of possible steric hindrance. Soluble or aggregated SOD1 with or without Alexa555 modifications was incubated in a buffer containing 4 M urea and 5 mM TCEP, where SOD1 aggregates are redissolved and any disulfide bonds are reduced. These SOD1 samples were then digested by lysyl endopeptidase and analyzed by MALDI-TOF mass spectrometry.

Among the mass peaks obtained, we have noted four proteolytic fragments, in particular Ala^4–Lys^{23} (*m/z* 2115.1, monoisotopic, 2143.2 for A4V), Gly^{37}–Lys^{70} (*m/z* 3592.9, average, 3692.1 for G37R), His^{71}–Lys^{122} (*m/z* 5479.0, average), and Thr^{137}–Gln^{153} (*m/z* 1587.8, monoisotopic, 1575.8 for I149T), for identification of Alexa555 modification at Cys^6, Cys^{57}, Cys^{111}, and Cys^{146}, respectively. Alexa555 modification adds 955.3 Da to the mass of the corresponding peptide. In soluble WT SOD1, mass peaks derived from the Alexa555-modified peptides (Gly^{37}–Lys^{70}, His^{71}–Lys^{122}, and Thr^{137}–Gln^{153}) were observed (*left panels* in Fig. 3, *B–D*), indicating that Alexa555 can access Cys^{57}, Cys^{111}, and Cys^{146}. L126X, which is a truncated SOD1 at Leu^{126}, does not produce a Thr^{137}–Gln^{153} peptide (*left panel* in Fig. 3*D*). When WT SOD1 forms aggregates, the Alexa555-modified peptide spanning from Thr^{137} to Gln^{153} was no longer observed (*right panel* in Fig. 3*D*), whereas a mass peak from the corresponding unmodified peptide was detected (supplemental Fig. S4*B*). This result suggests that Cys^{146} becomes buried and not accessible by Alexa555 upon aggregation of WT SOD1. No modification of Alexa555 at Cys^{146} was also seen in A4V and G37R aggregates (*right panel* in Fig. 3*D* and supplemental Fig. S4*B*) and supports our findings that region C containing Cys^{146} constitutes a core structure of types I (WT) and II (A4V and G37R) aggregates (Fig. 2). In contrast, an Alexa555-modified peptide (Thr^{137}–Gln^{153}) was observed in I149T aggregates (*right panel* in Fig. 3*D*), which is consistent with no involvement of region C in a core structure of type IV fibrils (Fig. 2). A similar pattern of mass peaks was obtained between WT and A4V, but it is notable that A4V aggregates exhibit significantly larger peak intensity of the Alexa555-modified peptide (His^{71}–Lys^{122}) containing Cys^{111} than the other aggregates (*right panel* in Fig. 3*C*). This would be described by no involvement of region B in a core structure of A4V aggregates (Fig. 2). In all five SOD1 aggregates tested, Cys^{57} but not Cys^6 is modified by Alexa555 (*right panel* in Fig. 3, *A* and *B*), but the corresponding unmodified peptide containing Cys^6 was detected (supplemental Fig. S4*A*), which is again consistent with our findings that Cys^6 but not Cys^{57} is involved in core structures of all four types of SOD1 aggregates (Fig. 2).

Mutation-dependent Polymorphism of SOD1 Fibrillar Aggregates—Given that a core structure is a building block of SOD1 aggregates, we expect that the aggregate morphology is also affected by mutation-dependent core structures. Although all mutant SOD1 aggregates tested here are fibrillar, the difference of fibril width is remarkable among mutant SOD1s (Fig. 4, *A–K*, and Table 1). For example, types I (*WT* and *L144F*, Fig. 4, *A* and *J*) and IV (*L126X* and *I149T*, Fig. 4, *I* and *K*) form relatively thicker fibrils (8–10 nm of its width) than the other mutant SOD1s, in which most of type II (*A4V*, *G37R*, and *G41S*, Fig. 4, *B*, *C*, and *E*) fibrils and type III (*G93R*, Fig. 4*H*) fibrils have ~3 nm of the width. In G41D, H46R, and G85R (Fig. 4, *D*, *F* and *G*), it appears that thin fibers are stacked to form intertwined and thicker fibrils with complex shapes; therefore, the widths of these fibrils are difficult to examine. Although there will be other structural/environmental factors regulating morphologies of SOD1 aggregates, we have suggested that mutation-dependent core structures contribute to produce a variety of aggregate morphologies.

New Biochemical Assay Method Reveals Mutation-dependent Solubility of SOD1 Aggregates—Our next question is whether any biochemical aspects of an SOD1 aggregate are affected by its structural polymorphism. In general, protein aggregates are insoluble in a physiological buffer solution, but addition of detergents to a buffer solution enhances solubility of aggregates. It has been reported that *in vivo* SOD1 aggregates purified from spinal cords of amyotrophic lateral sclerosis model mice are soluble in the presence of detergent SDS but not Nonidet P-40 (26). As shown in Fig. 5*A*, we have confirmed that our *in vitro* aggregates of WT apo-$SOD1^{SH}$ were not solubilized by 1% Nonidet P-40 but were completely soluble in the presence of 1% SDS. This is also the case in L126X apo-$SOD1^{SH}$ aggregates (Fig. 5*A*). Interestingly, when we tested another detergent called *N*-lauroylsarcosine (Sarkosyl), both WT and L126X aggregates were partially solubilized and exhibited different degrees of solubilization as follows: ~20 and 40% in WT and L126X aggregates, respectively (Fig. 5*A*). We have thus noted solubility of aggregates in a Sarkosyl-containing buffer as a mutation-dependent biochemical feature of SOD1 aggregates.

We have further found that temperature is another factor to regulate the solubility of SOD1 aggregates in a Sarkosyl-containing buffer. As shown in Fig. 5*B*, increasing amounts of SOD1 aggregates become solubilized at higher temperatures, but the temperature dependence of solubilization is different between WT and L126X aggregates. For example, L126X aggregates are almost completely solubilized at 60 °C, where half-amounts of WT aggregates are still found in an insoluble

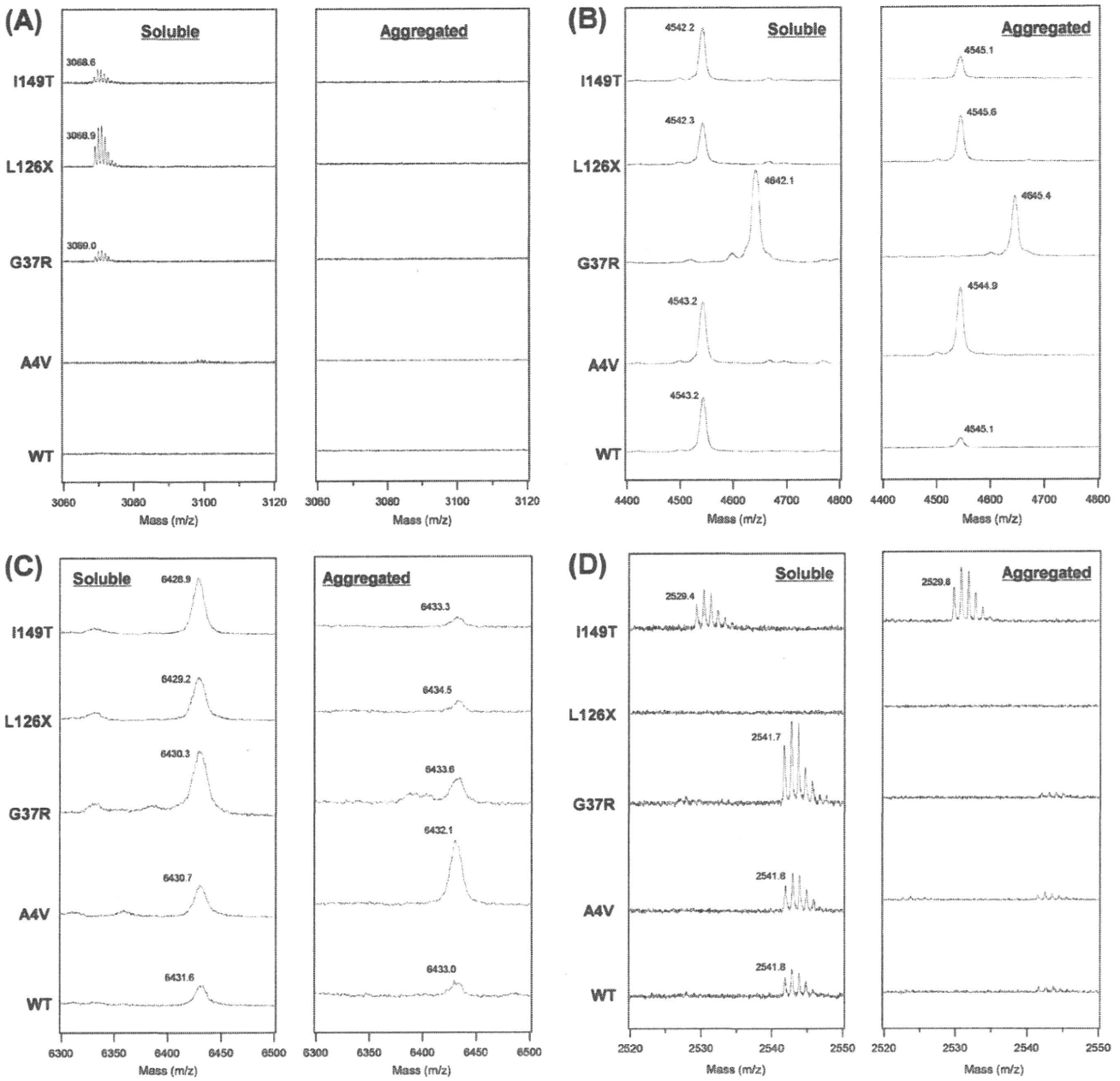

FIGURE 3. **Identification of SOD1 Cys residues that are modified with Alexa555.** Alexa555-modified SOD1 (WT, A4V, G37R, L126X, or I149T) was digested with lysyl endopeptidase, and mass peaks from the following Cys-containing peptides modified with Alexa555 are shown: *A*, Ala^4–Lys^{23} (Cys^6) with an Alexa555; *B*, Gly^{37}–Lys^{70} (Cys^{57}) with an Alexa555; *C*, His^{71}–Lys^{122} (Cys^{111}) with an Alexa555; and *D*, Thr^{137}–Gln^{153} (Cys^{146}) with an Alexa555. In each panel, proteolytic digestion was performed using either soluble (*left*) or aggregated (*right*) SOD1 modified with Alexa555. Observed mass was shown in each spectrum, and calculated mass values of Alexa555-modified peptides are as follows: 3070.4 in Ala^4–Lys^{23} (3098.5 for A4V), 4548.2 in Gly^{37}–Lys^{70} (4647.3 for G37R), 6434.3 in His^{71}–Lys^{122}, and 2543.1 in Thr^{137}–Gln^{153} (2531.1 for I149T). All of these mass peaks were not observed in unmodified SOD1 samples, confirming that the mass peaks shown in *A–D* are derived from Alexa555-modified peptides.

pellet fraction. For quantitative analysis, we have defined $T_{1/2}$ as temperature required for solubilization of half-amounts of aggregates. Table 1 summarizes $T_{1/2}$ values of fALS-mutant SOD1 aggregates, which can be approximated by fitting the data (Fig. 5*C*) with a sigmoidal function (see "Experimental Procedures"). Among the fALS-mutant SOD1 proteins tested here, $T_{1/2}$ was found to range from 42 °C (I149T) to 68 °C (L144F). We have also confirmed that *in vivo* SOD1 aggregates extracted from murine spinal cords also exhibit comparable temperature dependence of solubility to those of the *in vitro* ones; fractions of solubilized SOD1 in 1% Sarkosyl increases from around 30% (at 37 °C) to almost 100% (at 100 °C) (Fig. 5*D*).

According to our structural classification of SOD1 aggregates, we have found that type IV fibrils (L126X and I149T) exhibit significantly lower $T_{1/2}$ than the other types (Fig. 5*E*). In type IV, region C is not involved in a core structure of aggregates (Fig. 2), suggesting a role of region C in increasing insolubility of SOD1 fibrils. Indeed, types I and III aggregates, in

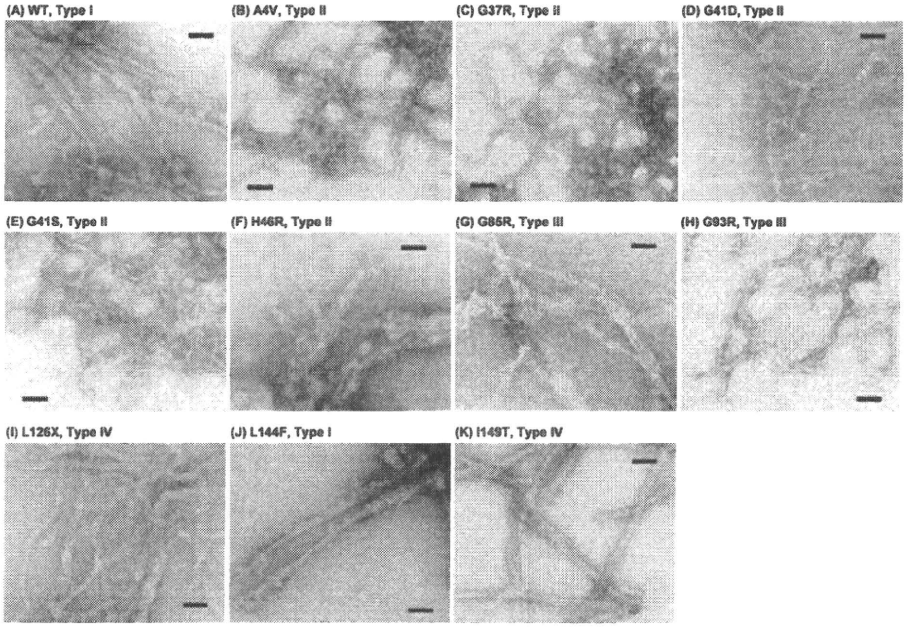

FIGURE 4. **Electron micrograms of (*A*) WT and (*B–K*) fALS-mutant SOD1 aggregates.** A *bar* in each panel represents 50 nm.

which regions A–C form a core structure (Fig. 2), have higher $T_{1/2}$ than type IV (Fig. 5*E*). Accordingly, mutation-dependent interactions among regions A–C would regulate physical properties of SOD1 aggregates such as solubility.

DISCUSSION

Mutations in SOD1 have been identified as a cause of fALS, and insoluble aggregation of mutant SOD1 proteins is a common pathological change in this disease (10). We previously proposed a molecular mechanism of SOD1 aggregation, in which either metallation or disulfide formation in SOD1 completely suppresses its fibrillar aggregation (13). Furthermore, several groups including us have reported that a role of fALS mutations in facilitating SOD1 aggregation is to decrease the affinity for zinc ions and retard disulfide formation (13–15). Although significant structural changes of an SOD1 molecule have been assumed upon aggregate formation, it remains an open question how SOD1 changes its structure to form fibrillar aggregates. Here, we have identified a core structure in SOD1 aggregates and extended our SOD1 aggregation model to include a polymorphism of fALS-mutant SOD1 aggregates (Fig. 6).

Molecular Mechanism to Produce Structurally Distinct SOD1 Aggregates—Based upon this study, it is likely that SOD1 aggregation occurs through unique and non-native interaction among three major parts of SOD1 (regions A–C, see Figs. 2 and 6). As mentioned in our previous study (13), a CD spectrum has suggested that SOD1 aggregates are composed mainly of β-sheet structures. Soluble apo-SOD1^{SH} is also rich in β-sheets with an immunoglobulin fold (almost the same with Fig. 1*B*) but exhibits a CD spectrum different from that of SOD1 aggregates, suggesting significant structural changes of SOD1 upon its aggregation (13). Indeed, molecular dynamics simulations of WT SOD1 have proposed a domain swapping model in which drastic rearrangement of β-sheets leads to aggregation (18). In this model, non-native interactions possibly leading to aggregation occur among Ala^{1}–Glu^{40}, Glu^{100}–His^{120}, and the C termini, which correspond to regions A–C in this study, respectively (Fig. 1*A*). *In silico* and our *in vitro*/*in vivo* results have thus indicated that aggregation of SOD1 occurs not through a simple pile of apo-SOD1^{SH} monomers but through rearrangement of β-sheets in an SOD1 molecule to realize non-native interactions among regions A–C (Fig. 6).

When a core in the aggregate contains fALS mutations (*i.e.* A4V, L126X, L144F, and I149T), non-native interactions among regions A–C will be affected. A computer algorithm, TANGO (27), predicts that A4V and L144F mutations increase aggregation propensities of regions A and C, respectively. These changes may describe formation of a distinct aggregation core in A4V (Fig. 2) or significantly high $T_{1/2}$ of L144F aggregates (Fig. 5*E*). In I149T, an aggregation propensity of region C is predicted to significantly decrease (27), which is consistent with no involvement of region C in the core structure of I149T aggregates (Fig. 2). In addition, SOD1 forms type IV fibrils when truncated at Leu^{126} (L126X), confirming that region C is dispensable for formation of the aggregation core. However, it remains obscure how a distinct aggregation core is realized in the other SOD1s in which fALS mutations are located outside the core regions. Recent studies have suggested mutation-dependent structural dynamics of SOD1 (28, 29), which may be an important determinant for unique interactions among the core regions. We thus suppose that fALS mutations can directly or indirectly control non-native interactions among regions A–C and lead to formation of a distinct structure of SOD1 fibrils. Furthermore, in a native state of SOD1, regions A–C contain amino acid residues involved in dimerization, metal binding, and disulfide formation, respectively (Fig. 6). These post-translational processes therefore prohibit non-native interactions among regions A–C and suppress SOD1 aggregation, which is consistent with our previous studies (13).

Potential Roles of Structural Polymorphism of SOD1 Aggregates in Heterogeneous Phenotypes and Pathologies of fALS—Increasing evidence has suggested that a molecular structure of protein aggregates is tightly linked to a phenotype (5). For example, in transmissible spongiform encephalopathies, multiple strains with distinct disease phenotypes exist (2), and the emergence of such strains has been described by structural differences in fibrillar aggregates of a prion protein (3). Another example can be found in a neurodegenera-

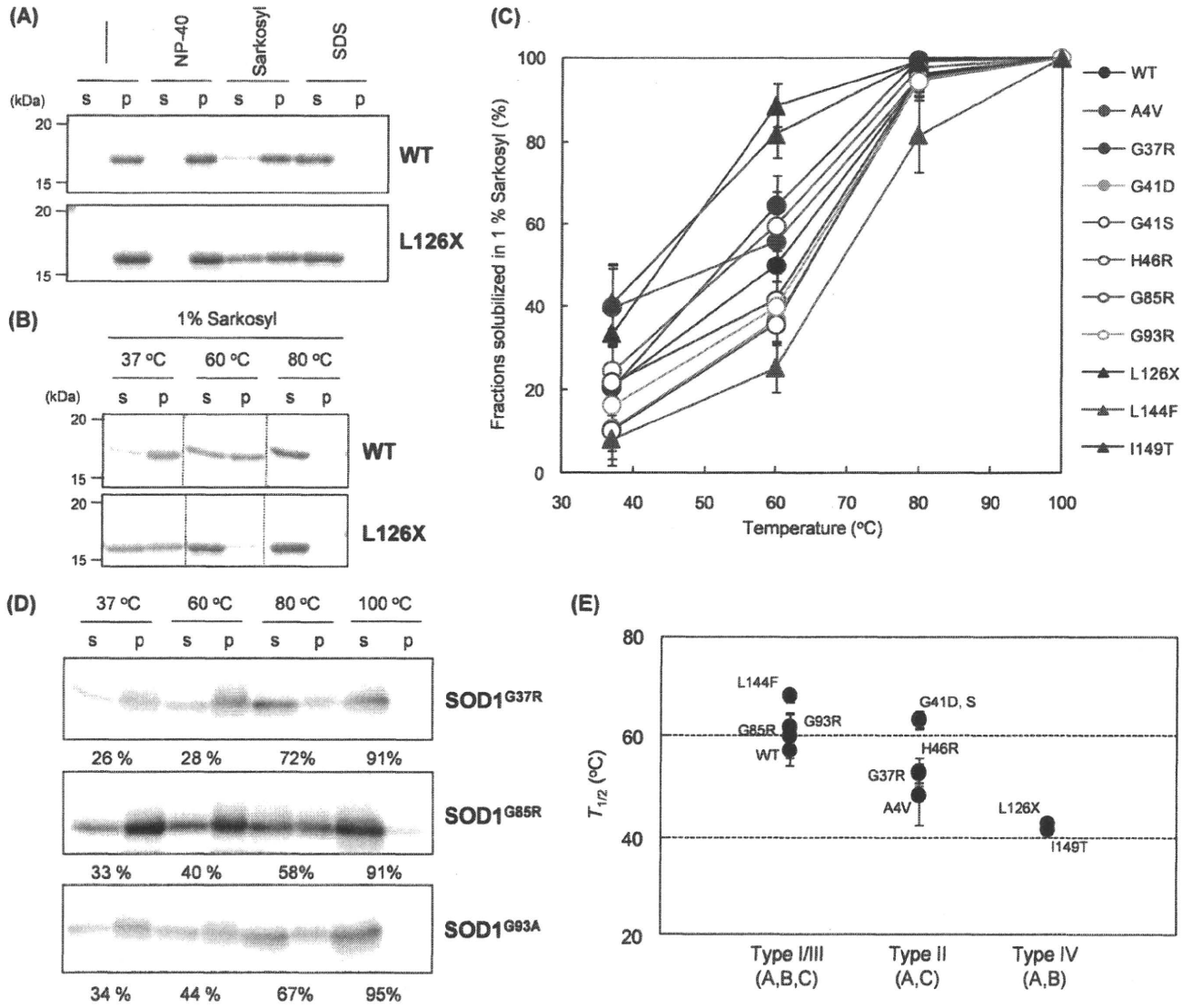

FIGURE 5. **Distinct solubility of SOD1 aggregates with different fALS mutations in the presence of Sarkosyl.** *A*, 2 μg of WT or L126X SOD1 aggregates were prepared in an NNE buffer with or without a detergent; either 1% Nonidet P-40 (*NP-40*), 1% Sarkosyl, or 1% SDS. After incubation at 37 °C for an hour, samples were ultracentrifuged at 110,000 × *g* for 30 min, and a supernatant (*s*) and a pellet (*p*) fraction were analyzed by a 12.5% SDS-polyacrylamide gel. *B*, temperature dependence of the WT or L126X aggregate solubility in the presence of 1% Sarkosyl. Experimental conditions were the same as described in *A* except the incubation temperature. *C*, effects of temperature on the aggregate solubility were further tested in all of the other fALS mutant SOD1 proteins, and fractions of solubilized SOD1 were estimated from its relative band intensities between supernatant and pellet on an SDS-polyacrylamide gel and plotted against incubation temperature. *D*, SOD1 aggregates were extracted from lumbar spinal cords of transgenic mice expressing G37R, G85R, and G93A SOD1 and incubated for an hour at indicated temperature in NNE buffer containing 1% Sarkosyl and 5 mM DTT. After ultracentrifugation at 110,000 × *g* for 30 min, supernatant (*s*) and pellet (*p*) fractions were probed by Western blotting analysis using sheep anti-SOD1 polyclonal antibody (Calbiochem). Percentages indicated *below* each gel image represent the fraction of solubilized SOD1 that is estimated from band intensities. *E*, $T_{1/2}$ was obtained by fitting the data in *C* with a sigmoidal function (see "Experimental Procedures") and plotted against fibril types defined in this study.

tive disease collectively called tauopathies, in which a microtubule-binding protein, Tau, forms insoluble fibrillar aggregates (30). Tauopathies include Alzheimer disease, Pick disease, and others; in each of these tauopathies, Tau forms fibrils with distinct morphologies such as paired helical filaments in Alzheimer disease and straight filaments in Pick disease (30). Importantly, albeit with less attention, different fALS mutations in SOD1 also associate with distinct disease phenotypes such as severity and age of disease onset (19, 31, 32). For example, duration of the disease depends upon fALS mutations and ranges from less than a year to more than 20 years (32). Because symptomatic changes follow appearance of SOD1 inclusions in fALS patients and rodent models (33), a possible mutation dependence of SOD1 aggregate structures may be relevant in understanding phenotypic heterogeneity in fALS.

Among SOD1 mutations examined here, there seems no correlation of disease onset with disease duration (Fig. 6, *inset*; Table 1) (31, 32). Based upon our structural classification of SOD1 aggregates, type IV aggregates seem to associate with relatively early onset and short duration of disease (Fig. 6, *inset*). Also, later disease-onset would be expected in

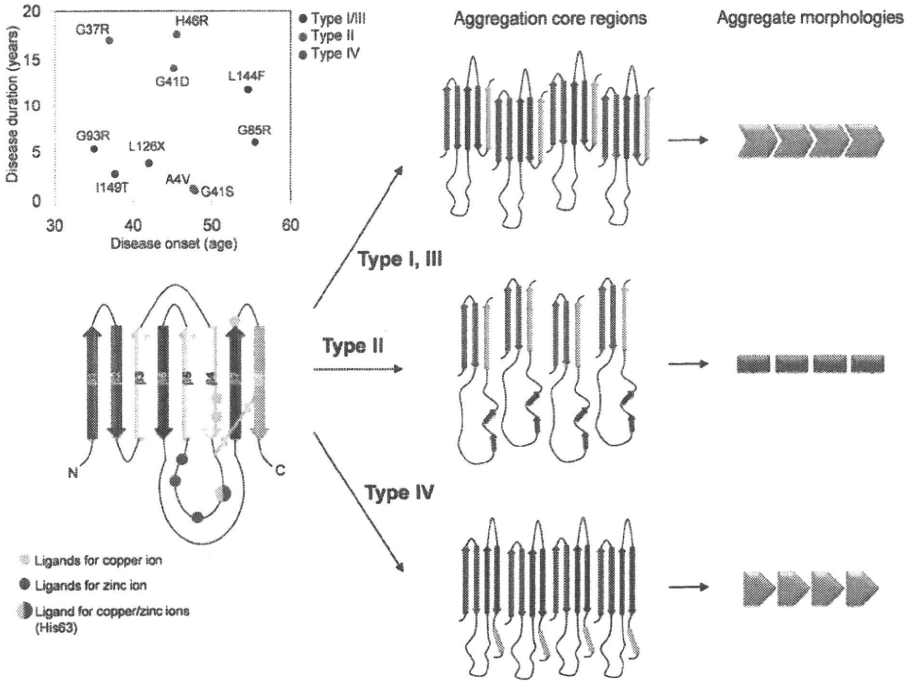

FIGURE 6. **Our proposed model to describe mutation-dependent structural polymorphism of SOD1 aggregates.** In secondary structural representation of SOD1 (*left*), regions A–C are colored *red*, *blue* and *green*, respectively. Rearrangement of these regions results in the formation of a core, and at least three different combinations of interactions among regions A–C are possible (*middle*). An exact alignment of β-sheets in the aggregates remains unknown; therefore, alignment of regions A–C in each schematic representation (*middle*) is still speculative. Interactions among aggregation core regions determine overall morphologies (*right*) and biochemical properties of SOD1 aggregates. *Inset*, average disease duration is plotted against average onset of disease. Data were taken from Refs. 31, 32. Type I/III, II, and IV aggregates are colored by *black*, *red*, and *blue*, respectively.

type I/III mutant (L144F and G85R) and WT, but obviously the effects of the structural polymorphism of aggregates on disease phenotypes still need further investigations. For example, A4V and H46R mutations are well known to exhibit very severe and mild progression of the disease, respectively (32), but these two mutant SOD1 aggregates are categorized into the same type (type II) in our classification. Many biophysical factors such as affinity for metal ions (13) as well as protein structural stability (11) regulate the kinetics of SOD1 aggregation, which would further affect some of the disease phenotypes (34). Our *in vitro* and *in vivo* data therefore support roles of fALS mutations in structural and biochemical properties of SOD1 aggregates but also show that aggregate structure is not the only decisive factor regulating disease phenotypes.

Furthermore, it is notable that morphologies of SOD1 inclusions are variable among transgenic mice expressing human SOD1 with different fALS mutations (33). For example, formation of SOD1 inclusions is a major change in H46R and G85R SOD1 transgenic mice, although in G37R and G93A SOD1 severe mitochondrial damage is observed with lesser amounts of SOD1 inclusions (35, 36). In addition, thioflavin S, a fluorescent dye upon binding with amyloid-like fibrils, can stain SOD1 inclusions in G37R, G85R, and G93A (13, 37) but not L126X transgenic mice (38). Also in a *Caenorhabditis elegans* model, morphologically and biophysically distinct classes of mutant SOD1 aggregates have been found (39); FRAP analysis shows higher mobility of L126X aggregates than those of G85R and G93A aggregates in the body wall muscle cells. All these *in vivo* studies have thus suggested that fALS mutations affect structural properties of pathological SOD1 aggregates, and this study will provide a molecular basis to describe mutation-dependent structural and biochemical properties of SOD1 aggregates.

In summary, we have revealed mutation-dependent structural polymorphism of SOD1 aggregates. Multiple regions in a single SOD1 protein are responsible for formation of a core upon its fibrillar aggregation. We have further found that morphologies as well as biochemical properties of SOD1 aggregates are affected by a combination of interactions among the aggregate core regions (Fig. 6). In analogy with a protein folding process, we suppose that variable structures of protein aggregates are possible by alternatively or non-natively "folding" the peptide fragments involved in the core of aggregates. Disease-causing mutations would regulate such non-native folding pathways to form a distinct structure of protein aggregates and exert distinct cytotoxicity. Given that several regions within a single protein sequence are often predicted to have high aggregation propensities (27), our proposing model (Fig. 6) would be a general mechanism producing structural polymorphism in the aggregates of many other proteins.

Acknowledgments—We thank Dr. Shoji Watanabe for fruitful discussions. We also thank the Support Unit for Bio-material Analysis; RIKEN BSI Research Resources Center, especially Masaya Usui and Kaori Otsuki, for mass analysis; and Yuriko Sakamaki for electron micrographic observations.

REFERENCES

1. Chiti, F., and Dobson, C. M. (2006) *Annu. Rev. Biochem.* **75,** 333–366
2. Bruce, M. E., and Fraser, H. (1991) *Curr. Top. Microbiol. Immunol.* **172,** 125–138
3. Jones, E. M., and Surewicz, W. K. (2005) *Cell* **121,** 63–72
4. Nekooki-Machida, Y., Kurosawa, M., Nukina, N., Ito, K., Oda, T., and Tanaka, M. (2009) *Proc. Natl. Acad. Sci. U.S.A.* **106,** 9679–9684
5. Tanaka, M., Chien, P., Naber, N., Cooke, R., and Weissman, J. S. (2004) *Nature* **428,** 323–328
6. Rosen, D. R., Siddique, T., Patterson, D., Figlewicz, D. A., Sapp, P., Hentati, A., Donaldson, D., Goto, J., O'Regan, J. P., Deng, H. X., *et al.* (1993) *Nature* **362,** 59–62
7. McCord, J. M., and Fridovich, I. (1969) *J. Biol. Chem.* **244,** 6049–6055
8. Furukawa, Y., Torres, A. S., and O'Halloran, T. V. (2004) *EMBO J.* **23,** 2872–2881

9. Reaume, A. G., Elliott, J. L., Hoffman, E. K., Kowall, N. W., Ferrante, R. J., Siwek, D. F., Wilcox, H. M., Flood, D. G., Beal, M. F., Brown, R. H., Jr., Scott, R. W., and Snider, W. D. (1996) *Nat. Genet.* **13,** 43–47
10. Bruijn, L. I., Miller, T. M., and Cleveland, D. W. (2004) *Annu. Rev. Neurosci.* **27,** 723–749
11. Furukawa, Y., and O'Halloran, T. V. (2005) *J. Biol. Chem.* **280,** 17266–17274
12. Rodriguez, J. A., Shaw, B. F., Durazo, A., Sohn, S. H., Doucette, P. A., Nersissian, A. M., Faull, K. F., Eggers, D. K., Tiwari, A., Hayward, L. J., and Valentine, J. S. (2005) *Proc. Natl. Acad. Sci. U.S.A.* **102,** 10516–10521
13. Furukawa, Y., Kaneko, K., Yamanaka, K., O'Halloran, T. V., and Nukina, N. (2008) *J. Biol. Chem.* **283,** 24167–24176
14. Hayward, L. J., Rodriguez, J. A., Kim, J. W., Tiwari, A., Goto, J. J., Cabelli, D. E., Valentine, J. S., and Brown, R. H., Jr. (2002) *J. Biol. Chem.* **277,** 15923–15931
15. Jonsson, P. A., Graffmo, K. S., Andersen, P. M., Brännström, T., Lindberg, M., Oliveberg, M., and Marklund, S. L. (2006) *Brain* **129,** 451–464
16. Hörnberg, A., Logan, D. T., Marklund, S. L., and Oliveberg, M. (2007) *J. Mol. Biol.* **365,** 333–342
17. Teilum, K., Smith, M. H., Schulz, E., Christensen, L. C., Solomentsev, G., Oliveberg, M., and Akke, M. (2009) *Proc. Natl. Acad. Sci. U.S.A.* **106,** 18273–18278
18. Khare, S. D., Wilcox, K. C., Gong, P., and Dokholyan, N. V. (2005) *Proteins* **61,** 617–632
19. Andersen, P. M., Nilsson, P., Keränen, M. L., Forsgren, L., Hägglund, J., Karlsborg, M., Ronnevi, L. O., Gredal, O., and Marklund, S. L. (1997) *Brain* **120,** 1723–1737
20. Boillée, S., Yamanaka, K., Lobsiger, C. S., Copeland, N. G., Jenkins, N. A., Kassiotis, G., Kollias, G., and Cleveland, D. W. (2006) *Science* **312,** 1389–1392
21. Bruijn, L. I., Becher, M. W., Lee, M. K., Anderson, K. L., Jenkins, N. A., Copeland, N. G., Sisodia, S. S., Rothstein, J. D., Borchelt, D. R., Price, D. L., and Cleveland, D. W. (1997) *Neuron* **18,** 327–338
22. Gurney, M. E., Pu, H., Chiu, A. Y., Dal Canto, M. C., Polchow, C. Y., Alexander, D. D., Caliendo, J., Hentati, A., Kwon, Y. W., and Deng, H. X. (1994) *Science* **264,** 1772–1775
23. Shaw, B. F., Lelie, H. L., Durazo, A., Nersissian, A. M., Xu, G., Chan, P. K., Gralla, E. B., Tiwari, A., Hayward, L. J., Borchelt, D. R., Valentine, J. S., and Whitelegge, J. P. (2008) *J. Biol. Chem.* **283,** 8340–8350
24. Wischik, C. M., Novak, M., Thøgersen, H. C., Edwards, P. C., Runswick, M. J., Jakes, R., Walker, J. E., Milstein, C., Roth, M., and Klug, A. (1988) *Proc. Natl. Acad. Sci. U.S.A.* **85,** 4506–4510
25. Ghadge, G. D., Wang, L., Sharma, K., Monti, A. L., Bindokas, V., Stevens, F. J., and Roos, R. P. (2006) *Neurobiol. Dis.* **21,** 194–205
26. Wang, J., Slunt, H., Gonzales, V., Fromholt, D., Coonfield, M., Copeland, N. G., Jenkins, N. A., and Borchelt, D. R. (2003) *Hum. Mol. Genet.* **12,** 2753–2764
27. Fernandez-Escamilla, A. M., Rousseau, F., Schymkowitz, J., and Serrano, L. (2004) *Nat. Biotechnol.* **22,** 1302–1306
28. Molnar, K. S., Karabacak, N. M., Johnson, J. L., Wang, Q., Tiwari, A., Hayward, L. J., Coales, S. J., Hamuro, Y., and Agar, J. N. (2009) *J. Biol. Chem.* **284,** 30965–30973
29. Shaw, B. F., Durazo, A., Nersissian, A. M., Whitelegge, J. P., Faull, K. F., and Valentine, J. S. (2006) *J. Biol. Chem.* **281,** 18167–18176
30. Lee, V. M., Goedert, M., and Trojanowski, J. Q. (2001) *Annu. Rev. Neurosci.* **24,** 1121–1159
31. Prudencio, M., Hart, P. J., Borchelt, D. R., and Andersen, P. M. (2009) *Hum. Mol. Genet.* **18,** 3217–3226
32. Wang, Q., Johnson, J. L., Agar, N. Y., and Agar, J. N. (2008) *PLoS Biol.* **6,** e170
33. Turner, B. J., and Talbot, K. (2008) *Prog. Neurobiol.* **85,** 94–134
34. Lindberg, M. J., Tibell, L., and Oliveberg, M. (2002) *Proc. Natl. Acad. Sci. U.S.A.* **99,** 16607–16612
35. Nagai, M., Aoki, M., Miyoshi, I., Kato, M., Pasinelli, P., Kasai, N., Brown, R. H., Jr., and Itoyama, Y. (2001) *J. Neurosci.* **21,** 9246–9254
36. Watanabe, M., Dykes-Hoberg, M., Culotta, V. C., Price, D. L., Wong, P. C., and Rothstein, J. D. (2001) *Neurobiol. Dis.* **8,** 933–941
37. Wang, J., Xu, G., Gonzales, V., Coonfield, M., Fromholt, D., Copeland, N. G., Jenkins, N. A., and Borchelt, D. R. (2002) *Neurobiol. Dis.* **10,** 128–138
38. Wang, J., Xu, G., Li, H., Gonzales, V., Fromholt, D., Karch, C., Copeland, N. G., Jenkins, N. A., and Borchelt, D. R. (2005) *Hum. Mol. Genet.* **14,** 2335–2347
39. Gidalevitz, T., Krupinski, T., Garcia, S., and Morimoto, R. I. (2009) *PLoS Genet.* **5,** e1000399

Neuron
Article

Misfolded Mutant SOD1 Directly Inhibits VDAC1 Conductance in a Mouse Model of Inherited ALS

Adrian Israelson,[1] Nir Arbel,[2] Sandrine Da Cruz,[1] Hristelina Ilieva,[1] Koji Yamanaka,[3] Varda Shoshan-Barmatz,[2] and Don W. Cleveland[1,*]

[1]Ludwig Institute for Cancer Research and Departments of Cellular and Molecular Medicine and Neurosciences, University of California at San Diego, La Jolla, CA 92093-0670, USA

[2]Department of Life Sciences and the National Institute for Biotechnology in the Negev, Ben-Gurion University of the Negev, Beer-Sheva 84105, Israel

[3]Laboratory of Motor Neuron Diseases, RIKEN Brain Science Institute, 2-1 Hirosawa, Wako-shi, Saitama 351-0198, Japan

*Correspondence: dcleveland@ucsd.edu

DOI 10.1016/j.neuron.2010.07.019

SUMMARY

Mutations in superoxide dismutase (SOD1) cause amyotrophic lateral sclerosis (ALS), a neurodegenerative disease characterized by loss of motor neurons. With conformation-specific antibodies, we now demonstrate that misfolded mutant SOD1 binds directly to the voltage-dependent anion channel (VDAC1), an integral membrane protein imbedded in the outer mitochondrial membrane. This interaction is found on isolated spinal cord mitochondria and can be reconstituted with purified components in vitro. ADP passage through the outer membrane is diminished in spinal mitochondria from mutant SOD1-expressing ALS rats. Direct binding of mutant SOD1 to VDAC1 inhibits conductance of individual channels when reconstituted in a lipid bilayer. Reduction of VDAC1 activity with targeted gene disruption is shown to diminish survival by accelerating onset of fatal paralysis in mice expressing the ALS-causing mutation $SOD1^{G37R}$. Taken together, our results establish a direct link between misfolded mutant SOD1 and mitochondrial dysfunction in this form of inherited ALS.

INTRODUCTION

Amyotrophic lateral sclerosis (ALS) is a progressive adult-onset neurodegenerative disorder characterized by the selective loss of upper and lower motor neurons in the brain and spinal cord (Cleveland and Rothstein, 2001). The typical age of onset is between 50 to 60 years, followed by paralysis and ultimately death within 2–5 years after onset (Mulder et al., 1986). Most instances of ALS are sporadic lacking any apparent genetic linkage, but 10% are inherited in a dominant manner. Twenty percent of these familial cases have been attributed to mutations in the gene encoding cytoplasmic Cu/Zn superoxide dismutase (SOD1) (Rosen et al., 1993). Although multiple hypotheses have been proposed to explain mutant SOD1-mediated toxicity (Ilieva et al., 2009), the exact mechanism(s) responsible for motor neuron degeneration remains unsettled.

Mitochondrial dysfunction has been proposed to contribute to disease pathogenesis. Histopathological observations of disturbed mitochondrial structure have been reported in muscle of both sporadic and familial ALS patients (Hirano et al., 1984a, 1984b; Sasaki and Iwata, 1996, 2007) and in mutant SOD1 mouse models expressing dismutase active (Dal Canto and Gurney, 1994; Higgins et al., 2003; Kong and Xu, 1998; Wong et al., 1995), but not inactive mutants (Bruijn et al., 1997). Moreover, functionality of mitochondria has been reported to be affected in spinal cord and skeletal muscles of human sporadic ALS or familial ALS patients (Dupuis et al., 2003; Echaniz-Laguna et al., 2002; Vielhaber et al., 1999; Wiedemann et al., 2002), as well as in some ALS mouse models (Damiano et al., 2006; Mattiazzi et al., 2002; Nguyen et al., 2009).

A proportion of the predominantly cytosolic SOD1 has been reported to localize to mitochondria in certain contexts. In both rodent models and patient samples, mutant SOD1 is present in fractions enriched for mitochondria derived from affected, but not unaffected, tissues (Bergemalm et al., 2006; Deng et al., 2006; Liu et al., 2004; Mattiazzi et al., 2002; Vande Velde et al., 2008; Vijayvergiya et al., 2005) and a clear temporal correlation between mitochondrial association and disease progression was shown for multiple mutant SOD1s (Liu et al., 2004). Purification of mitochondria, including floatation steps that eliminate protein only aggregates, coupled with protease accessibility has demonstrated mutant SOD1 deposition on the cytoplasmic-facing surface of spinal cord mitochondria (Liu et al., 2004; Vande Velde et al., 2008). Sensitivity to proteolysis and immunoprecipitation with an antibody specific for misfolded SOD1 further indicated that misfolded forms of dismutase active and inactive SOD1 are deposited onto the cytoplasmic face of the outer membrane of spinal cord mitochondria (Vande Velde et al., 2008). This is accompanied by altered accumulated levels of a few mitochondrial proteins, reduced import of multiple mitochondrial proteins, and reduced complex I activity (T. Miller, C. Vande Velde, and D.W.C., unpublished data).

Oxidative phosphorylation requires the transport of metabolites, including ADP, ATP, and inorganic phosphate across both mitochondrial membranes. Located in the outer mitochondrial membrane, the voltage-dependent anion channel (VDAC),

known as mitochondrial porin, assumes a crucial position in the cell, controlling metabolic cross-talk between the mitochondrion and the rest of the cell, thus regulating the metabolic and energetic functions of mitochondria (Shoshan-Barmatz et al., 2006, 2008). Of the three VDAC isoforms (VDAC1–3), VDAC1 is the most abundant in most cells. VDAC1 is a primary contributor to ATP/ADP flux across the outer mitochondrial membrane (Colombini, 2004; Lemasters and Holmuhamedov, 2006). Initially named somewhat misleadingly as a channel for anions, it is also responsible for import/export of Ca^{2+} (Gincel et al., 2001) and other cations (Benz, 1994; Colombini, 2004), adenine nucleotides (Rostovtseva and Colombini, 1997; Rostovtseva and Bezrukov, 1998) and other metabolites (Hodge and Colombini, 1997). Indeed, it has been demonstrated that silencing VDAC1 expression in a cultured cell line using shRNA resulted in reduced ATP production and a decrease in cell growth (Abu-Hamad et al., 2006).

VDAC1 is also a key player in mitochondria-mediated apoptosis. VDAC1 has been implicated in apoptotic-relevant events, due to serving as the target for members of the pro- and anti-apoptotic Bcl2-family of proteins (Arbel and Shoshan-Barmatz, 2010; Shimizu et al., 1999) and due to its function in the release of apoptotic proteins from the intermitochondrial membrane space (Abu-Hamad et al., 2009; Shoshan-Barmatz et al., 2006, 2008; Tajeddine et al., 2008). VDAC1 has also been implicated in Parkinson's disease as a direct target for Parkin-mediated poly-ubiquitylation and mitophagy (Geisler et al., 2010).

Starting from recognition that a proportion of misfolded, mutant SOD1 is bound to the cytoplasmic face of the outer membrane of mitochondria in affected tissues (Liu et al., 2004; Rakhit et al., 2007; Vande Velde et al., 2008), we now identify damage to spinal cord mitochondria to arise through direct binding of misfolded SOD1 onto the cytoplasmic-facing domain of VDAC1, thereby inhibiting its conductance.

RESULTS

Mutant SOD1 and VDAC1 Interact In Vivo in Spinal Cord of Transgenic SOD1 Rats

To investigate potential interactions between mutant SOD1 and VDAC1, mitochondria from rats expressing wild-type human SOD1 ($hSOD1^{wt}$) or either of two different ALS-linked SOD1 mutants, a dismutase active $hSOD1^{G93A}$ and a dismutase inactive $hSOD1^{H46R}$, were highly purified by repeated centrifugation steps (summarized in Figure 1A) including a final density gradient flotation step to eliminate any contaminating protein only aggregates (proteins sediment downward in these conditions because of their higher density), as previously described (Vande Velde et al., 2008). Immunoblotting of immunoprecipitates generated after addition of an SOD1 antibody to solubilized mitochondrial lysates revealed that a proportion of VDAC1 was coprecipitated with dismutase active and inactive mutant SOD1, but not wild-type SOD1 (Figure 1B). Parallel immunoprecipitations with a VDAC1 antibody confirmed coprecipitation of both $hSOD1^{G93A}$ and $hSOD1^{H46R}$ with VDAC1 (Figure 1D). Binding to VDAC1 was a property only of spinal cord mitochondria, as no association of mutant SOD1 was seen with purified brain mitochondria from the same animals using immunoprecipitation with SOD1 (Figure 1C) or VDAC1 (Figure 1E) antibodies. This latter finding is consistent with prior efforts that had demonstrated that mutant SOD1 associates with the cytoplasmic face of the outer membrane of mitochondria in spinal cord, but not other tissue types (Liu et al., 2004; Vande Velde et al., 2008). Moreover, mutant SOD1 binding to VDAC1 is inversely correlated with the level of hexokinase-I, a known partner that binds to VDAC1 exposed on the cytoplasmic mitochondrial surface (Abu-Hamad et al., 2008; Azoulay-Zohar et al., 2004; Zaid et al., 2005), with hexokinase accumulating to much higher level in brain than spinal cord mitochondria (Figure 1F).

Misfolded Mutant SOD1 Specifically Interacts with VDAC1 In Vivo in Spinal Cord of Transgenic SOD1 Rats

To test the nature of the interaction between mutant SOD1 and VDAC1, immunoprecipitation was performed with a SOD1 antibody that recognizes a "disease-specific epitope" (DSE) that is unavailable on correctly folded SOD1 (Cashman and Caughey, 2004; Paramithiotis et al., 2003; Urushitani et al., 2007), but is present on misfolded mutant SOD1s in inherited ALS (Rakhit et al., 2007). Using one such antibody (DSE2), age-dependent deposition of mutant SOD1 onto the cytoplasmic face of spinal cord mitochondria has been shown to reflect association of misfolded SOD1 (Vande Velde et al., 2008). We exploited this antibody to examine if the SOD1 associated with VDAC1 is bound through misfolded SOD1. Liver, brain, and spinal cord cytosolic and mitochondrial fractions purified from symptomatic rats expressing mutant $hSOD1^{G93A}$ were immunoprecipitated (see schematic in Figure 2A) with the DSE2 antibody, which recognizes an epitope in the electrostatic loop of hSOD1 (between residues 125–142) that is buried in normally folded SOD1. Misfolded mutant $SOD1^{G93A}$ was not detectable in the soluble fraction of any tissue, but was immunoprecipitated from the spinal cord, but not liver or brain, mitochondrial fractions (Figure 2B).

Solubilized spinal cord mitochondria purified from presymptomatic and symptomatic rats expressing either of two different SOD1 mutants, dismutase active $hSOD1^{G93A}$ and dismutase inactive $hSOD1^{H46R}$, as well as $hSOD1^{wt}$ were immunoprecipitated with the DSE2 antibody and coimmunoprecipitated components identified by immunoblotting. An age-dependent increase in misfolded SOD1 was seen for both mutants, with a significantly higher proportion of the dismutase inactive $SOD1^{H46R}$ in a misfolded conformation. In samples from symptomatic animals, VDAC1 coprecipitated together with the misfolded mutant SOD1, as revealed by immunoblotting of immunoprecipitates (Figure 2C). This association was selective for VDAC1, as misfolded mutant SOD1 did not coimmunoprecipitate with any of three other mitochondrial proteins examined (Figure 2C), including two additional outer mitochondrial membrane proteins with domains facing the cytoplasm: TOM40, the 40 kDa component of transport across the outer membrane (TOM) complex mediating all protein import from the cytoplasm to the mitochondria, and VDAC2, a second voltage-dependent anion channel isoform that has been estimated to represent 7% (kidney) to 25% (brain) of accumulated VDAC (Yamamoto

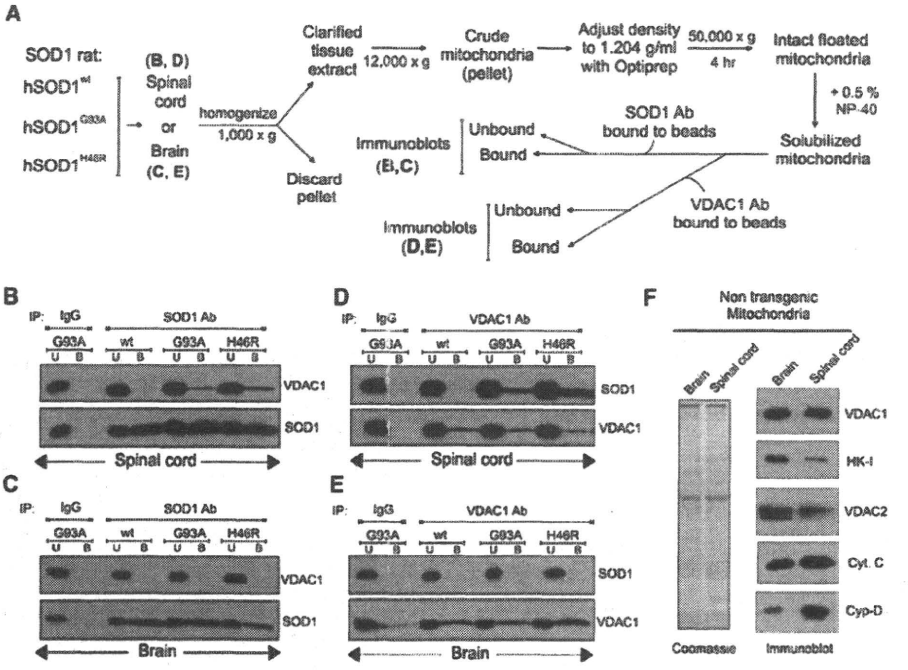

Figure 1. A Complex Containing Mutant SOD1 and VDAC1 from Spinal Cord Mitochondria

(A) Schematic outlining the different purification steps used. Floated isolated mitochondria from (B and D) hSOD1^{wt}, hSOD1^{G93A}, and hSOD1^{H46R} rat spinal cords or (C and E) brain were immunoprecipitated with (B and C) an SOD1 antibody or (D and E) VDAC1 antibody.

(B) Immunoblot of the SOD1 immunoprecipitates using VDAC1 antibody indicates that mutant SOD1 proteins hSOD^{G93A} and hSOD1^{H46R} coprecipitate VDAC1 (top). SOD1 immunoprecipitation was confirmed by reprobing the membrane with anti-SOD1 antibody (bottom).

(C) Immunoblots of SOD1 immunoprecipitates as in (B) except with brain mitochondria.

(D) Immunoprecipitation using VDAC1 antibody immunoblotted with SOD1 antibody (top). The membrane was then reprobed for VDAC1 (bottom).

(E) Immunoblots of VDAC1 immunoprecipitates as in (D), except with brain mitochondria. Abbreviations: U, unbound fraction (20%); B, bound fraction.

(F) Reduced hexokinase-I levels in spinal cord mitochondria. Polyacrylamide gel analysis of extracts of floated brain and spinal cord mitochondria. (Left) Coomassie stain; (right) immunoblot for VDAC1, hexokinase I (HK-I), VDAC2, cytochrome c (Cyt. C), and cyclophilin D (Cyp-D).

et al., 2006). It also did not coprecipitate cyclophilin-D, an important component of the permeability transition pore.

Furthermore, in order to determine which cells accumulate the misfolded form of SOD1, we performed immunostaining using the DSE2 antibody. Spinal cords from loxSOD1^{G37R} mice at different stages of the disease were subjected to immunostaining with DSE2 antibody (Figure 2D). The accumulation of misfolded SOD1 dramatically increased with disease progression. Although little accumulation of misfolded SOD1 is found by disease onset, it was preferentially found within motor neurons. During disease progression, a dramatic increase of misfolded SOD1 was apparently accumulated in other cells as well and probably also extracellularly. Throughout disease a proportion of the misfolded SOD1 was colocalized with mitochondria of motor neurons and other cells, starting at onset and increasing with disease progression (Figure 2D).

Binding of Mutant SOD1 Directly Inhibits VDAC1 Channel Conductance

To test if binding of mutant SOD1 affects VDAC1 function, VDAC1 was purified from spinal cords of nontransgenic rats (Figure 3A) and reconstituted into a planar lipid bilayer (Figure 3A) using conditions previously demonstrated to yield polarized VDAC1 membrane insertion such that the VDAC1 surface exposed on the *cis* side is the surface exposed to the cytosol when inserted into the mitochondrial outer membrane (Azoulay-Zohar et al., 2004; Israelson et al., 2005; Arbel and Shoshan-Barmatz, 2010). Activity of individual channels was measured as a function of time by the ions passing across the bilayer in response to an applied voltage gradient. This revealed that in the absence of SOD1, VDAC1 was stably in a fully open state (4 nS at 1 M KCl [Shoshan-Barmatz et al., 2006]) and remained so for extended periods.

Mutant SOD1 proteins hSOD1^{G93A}, hSOD1^{G85R}, as well as hSOD1^{wt}, were expressed using baculovirus and purified (Figure 3C; Hayward et al., 2002). Wild-type SOD1, even at the highest added concentration (8 μg/ml), had no effect on VDAC1 conductance when added on either *cis* or *trans* sides of the membrane (Figures 3E and 3I). However, addition of purified recombinant hSOD1^{G93A} or hSOD1^{G85R} (Figure 3C) substantially reduced VDAC1 channel conductance (Figures 3F and 3G). Both mutant SOD1s modified VDAC1 conductance only when added to the *cis* side (Figures 3F and 3G), but not the *trans* side (Figures 3J and 3K) of the bilayer, indicating that mutant SOD1 interacts

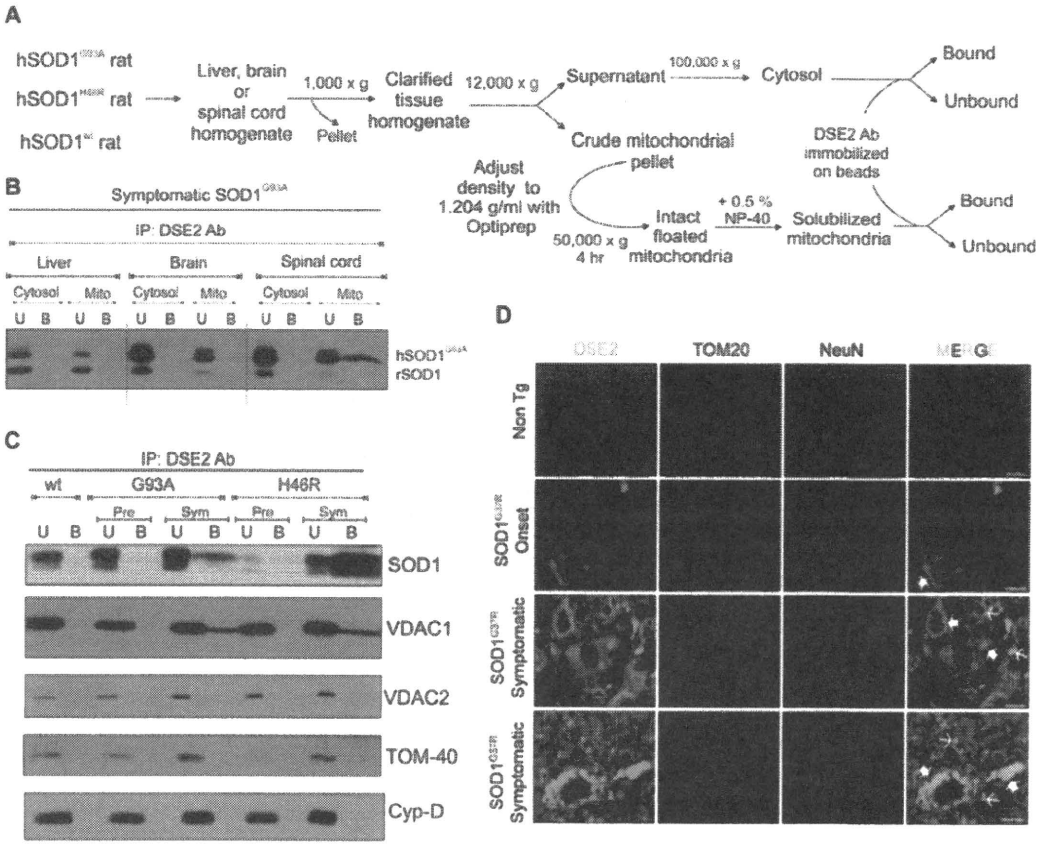

Figure 2. The Misfolded Mutant SOD1 Specifically Coprecipitates with VDAC1 in Spinal Cord Mitochondria

(A) Schematic showing the isolation of cytosolic and mitochondrial fractions.

(B) Liver, brain, and spinal cord cytosolic, and mitochondrial fractions were purified from symptomatic rats expressing hSOD1^{G93A} and the fractions were subjected to immunoprecipitation using DSE2 (3H1), a monoclonal antibody only recognizing misfolded SOD1 (Vande Velde et al., 2008). The immunoprecipitates were immunoblotted using an SOD1 antibody.

(C) Isolated floated mitochondria from hSOD1^{wt}, hSOD1^{G93A}, and hSOD1^{H46R} rat spinal cords (from presymptomatic and symptomatic animals) were immunoprecipitated with DSE2 (3H1), and the immunoprecipitates were immunoblotted using VDAC1, VDAC2, TOM-40, and cyclophilin-D antibodies. SOD1 immunoprecipitation was confirmed by reprobing the membrane with an SOD1 antibody (top).

(D) Immunohistochemical detection of misfolded SOD1 using DSE2 antibody shows that misfolded SOD1 (green) colocalizes with TOM20 (red), a mitochondrial outer membrane protein in a subset of spinal cord neurons assessed using NeuN (blue), a neuronal marker as highlighted by filled arrows. DSE2 positive staining can be detected in some neurons at onset and significantly increases with the appearance of disease symptoms.

Of note DSE2 staining is not restricted to neuronal mitochondria but is also detected in nonneuronal cells and the extracellular space as shown with thin arrows. No DSE2 staining was detected in neurons of 1 year old nontransgenic control mice (Non Tg). Scale bar: 10 μm. Abbreviation: U, unbound fraction (20%); B, bound fraction; Pre, presymptomatic; Sym, symptomatic.

with what would correspond to the cytosolic face of VDAC1 inserted into the outer mitochondrial membrane. Use of multichannel recordings revealed that not only did mutant SOD1 significantly lower the maximum voltage gated conductance of individual channels, it also provoked a stable, reduced level of VDAC1 conductance at all applied voltages (Figures 3L–3N). In order to determine if this interaction is specific for mutant SOD1, the effect of another aggregating protein (α-synuclein) was tested on bilayers containing reconstituted VDAC1. Even when added to levels 25 times greater than an amount of mutant SOD1 that markedly affected VDAC1 conductance (Figures 3F and 3G), neither wild-type nor mutant α-synuclein affected VDAC1 channel activity at any voltage (Figure 1S).

ADP Transport across the Outer Mitochondrial Membrane Is Reduced in Spinal Cords of Mutant SOD1 Rats

Since both dismutase active and inactive SOD1 mutant proteins reduced VDAC1 channel conductance for K^+ and Cl^- (Figure 3), we next tested whether mitochondrial conductance across the outer mitochondrial membrane was affected in animals chronically expressing mutant SOD1. To do this, we examined the uptake into mitochondria of adenine nucleotides (Figure 4A) which are known to be transported by VDAC1 (Lemasters and Holmuhamedov, 2006; Rostovtseva and Colombini, 1997). Freshly isolated spinal cord and liver mitochondria from SOD1^{G93A} rats were incubated (for 1 min)

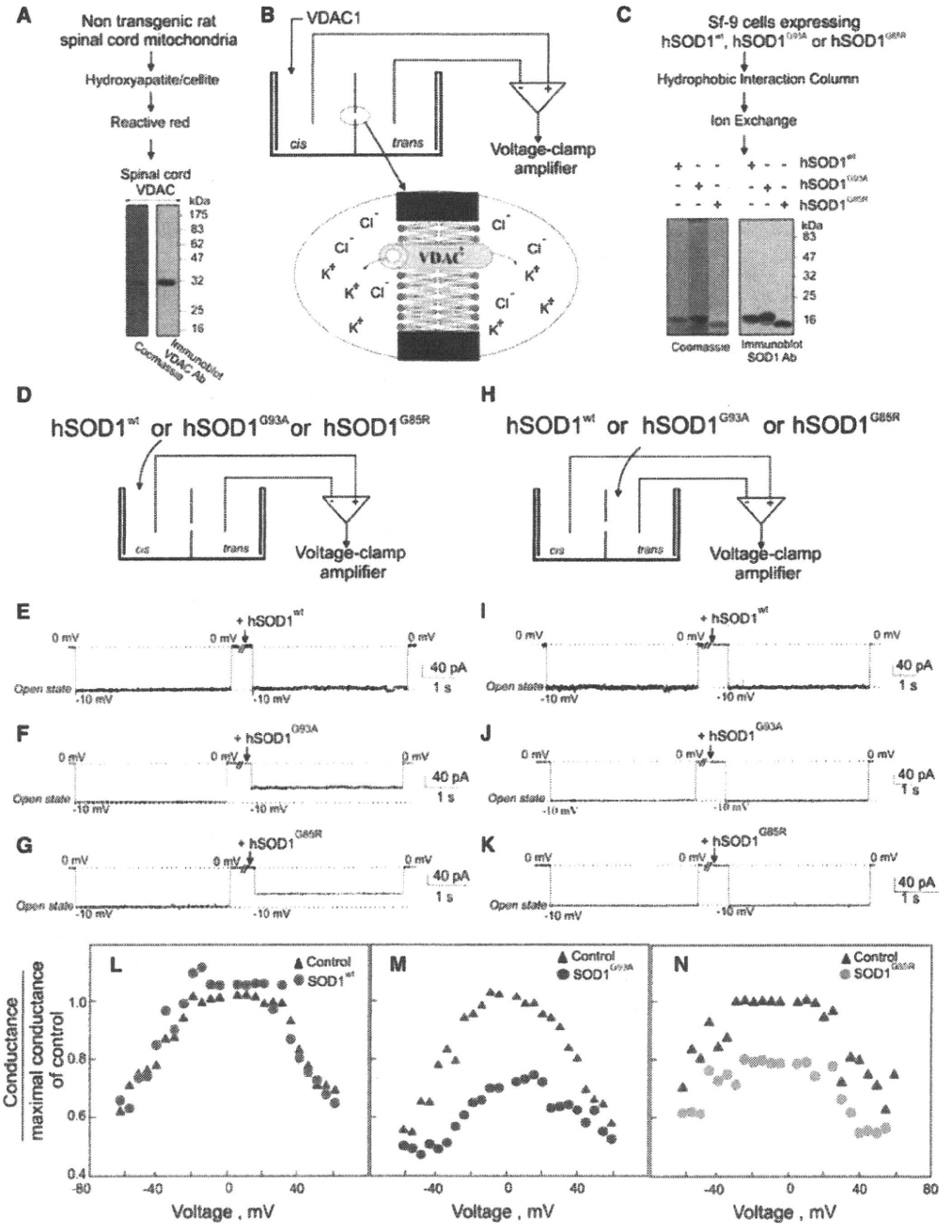

Figure 3. Mutant, but Not Wild-Type, SOD1 Interacts with Bilayer-Reconstituted VDAC1 to Reduce Its Channel Conductance

(A) Coomassie Blue staining and immunoblot of purified VDAC1 purified from rat spinal cord.

(B) Schematic presentation showing the planar lipid bilayer reconstitution and channel conductance assay system. Purified spinal cord VDAC1 was reconstituted into a planar lipid bilayer, and channel currents through VDAC1 were recorded.

(C) Coomassie Blue staining and immunoblot of purified recombinant $hSOD1^{wt}$, $hSOD1^{G93A}$, and $hSOD1^{G85R}$ expressed in insect cells using baculovirus.

(D–G) Currents through VDAC1 in response to a voltage step from 0 to −10 mV were recorded before and 2 min after the addition (to 2 μg/ml final) of purified recombinant (E) $hSOD1^{wt}$, (F) $hSOD1^{G93A}$, or (G) $hSOD1^{G85R}$ to the *cis* side of the bilayer.

(H–K) Currents through VDAC1 as in (D)–(G), except after SOD1 addition to the *trans* side of the bilayer. The dotted lines indicate current levels in the maximal and zero conductance states. These examples are representative of the results from 3–4 independent reconstitution experiments.

(L–N) Mutant SOD1 effect on VDAC1 channel activity at different voltages. Average steady-state conductance of VDAC1 before and after addition of (L) $hSOD1^{wt}$, (M) $hSOD1^{G93A}$, or (N) $hSOD1^{G85R}$, determined as a function of voltage with a multichannel recording.

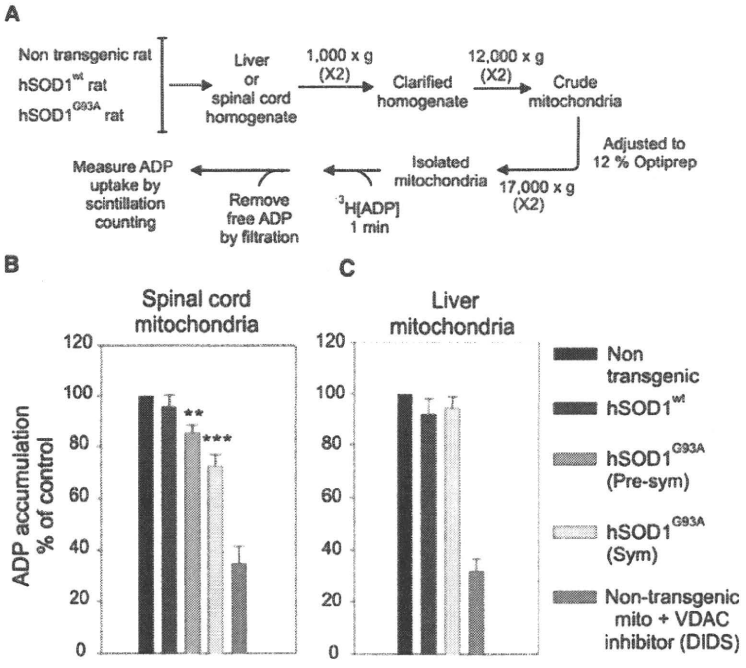

Figure 4. ADP Transport across the Outer Mitochondrial Membrane Is Reduced in Mitochondria from Spinal Cord of SOD1^{G93A} ALS Rats

(A) Schematic presentation of method for measuring ADP accumulation into isolated mitochondria as measured using radio-labeled [^{3}H]ADP.

(B and C) Mitochondria were isolated from (B) spinal cord and (C) liver of nontransgenic, hSOD1^{wt}, hSOD1^{G93A} presymptomatic, and hSOD1^{G93A} symptomatic rats. Student's t test was used and $p < 0.001$ (marked by three asterisks) and $p < 0.01$ (marked by two asterisks) were considered statistically significant. Values represent the means ± SEM of three to four independent experiments.

with radio-labeled [^{3}H]ADP and the amount of imported ADP was measured by scintillation counting after rapid filtration to remove the unincorporated ADP. Coincubation with 1 mM of the VDAC1 inhibitor DIDS (4, 4′-diisothiocyanostilbene-2, 2′-disulfonic acid) demonstrated that ~2/3 of the ADP uptake was through VDAC1 (Figures 4B and 4C). Compared to mitochondria from non-transgenic animals, uptake of ADP by spinal cord mitochondria from SOD1 mutant expressing animals was selectively and progressively inhibited, yielding ~40% inhibition of VDAC1-dependent uptake (~25% overall inhibition of ADP uptake) by a symptomatic stage (Figure 4B). Inhibition of ADP uptake was selective to spinal mitochondria as liver mitochondria from the same hSOD1^{G93A} animals retained normal ADP import at all ages examined (Figure 4C).

Mutant SOD1 Binding to Mitochondria In Vitro Diminishes ADP but Not Ca^{2+} Uptake

To test if inhibition of ADP import seen in spinal cord mitochondria from mutant SOD1 animals could be generated solely from mutant SOD1 binding to the cytoplasmic face of those mitochondria, purified recombinant SOD1 proteins (hSOD1^{wt}, hSOD1^{G93A}, and hSOD1^{G85R}) (Figure 3C) were added to mitochondria purified from spinal cords or livers of non transgenic rats (Figure 5A). Although a proportion of each of the recombinant SOD1s associated with both spinal cord and liver mitochondria (Figure 5D), accumulation of radio-labeled Ca^{2+} (presumably through the action of the mitochondrial calcium uniporter) into spinal cord or liver mitochondria was not affected by the addition of wild-type or mutant SOD1 (Figure 5C). On the other hand, VDAC1-mediated ADP accumulation into the same spinal cord or liver mitochondria was inhibited by both hSOD1^{G93A} and hSOD1^{G85R} mutants, but not hSOD1^{wt} (Figure 5B). This inhibition corresponded to a proportion of misfolded SOD1 associated with those mitochondria after incubation with either mutant, but not wild-type SOD1, as demonstrated by immunoprecipitation of intact mitochondria with the DSE2 antibody to misfolded SOD1 (Figure 5E). In contrast, wild-type SOD1 associated with the same mitochondria was not recognized by this misfolded SOD1 antibody (Figure 5E), consistent with its retention of normal folding and/or import into those mitochondria (Figure 5E).

Reduced VDAC1 Activity Diminishes Survival of Mutant SOD1^{G37R} Mice by Accelerating Disease Onset

Since we have established that (1) mutant SOD1 interacts directly with VDAC1 thereby inhibiting VDAC1 conductance (Figure 3), (2) spinal cord mitochondria from SOD1 mutant animals have progressive loss of ADP uptake, and (3) misfolded mutant SOD1 binds to normal mitochondria in vitro accompanied by selective loss of ADP conductance (Figure 5), we examined how reduced level and activity of VDAC1 affect disease course in SOD1^{G37R} mutant mice. To do this, we exploited mice heterozygous for disruption of the VDAC1 gene (producing what is effectively a null allele [Weeber et al., 2002]). These mice accumulate about half the normal level of VDAC1 protein (Figure 2S), while overall ADP conductance of spinal mitochondrial isolated from *VDAC1*$^{+/-}$ mice is reduced by ~25% (Figure 3S) relative to wild-type mice. After mating with SOD1^{G37R} mice, sex matched cohorts of mice and their littermates carrying the SOD1^{G37R} transgene and zero, one, or two active VDAC1 alleles were obtained and followed for disease onset, progression and survival. Measurement of ADP conductance of spinal mitochondria from *SOD1*^{G37R}/*VDAC1*$^{+/-}$ mice revealed a reduction to a level comparable to that corresponding to complete deletion of VDAC1 (Figure 3S).

A simple and objective measure of disease onset and early disease progression was applied by initiation of weight loss, reflecting denervation-induced muscle atrophy. While timing of progression from onset through either early (Figure 6E) or late (Figure 6F) disease phases was only modestly affected by reduction of VDAC1 levels, disease onset (Figures 6A and 6D) and